2017-12

Earthquakes as Precursors of Ductile Shear Zones in the Dry and Strong Lower Crust

Menegon, L

10.1002/2017GC007189
Geochemistry, Geophysics, Geosystems
American Geophysical Union

Earthquakes as precursors of ductile shear zones in the dry and strong lower crust

L. Menegon[1*], G. Pennacchioni[2], N. Malaspina[3], K. Harris[1†], and E. Wood[5‡]

[1]School of Geography, Earth and Environmental Sciences, Plymouth University, Drake Circus, PL4 8AA Plymouth, United Kingdom.

[2]Department of Geosciences, University of Padova, Via Gradenigo 6, I-35131 Padova, Italy.

[3]Department of Earth and Environmental Sciences, Università degli Studi di Milano Bicocca, Piazza della Scienza 4, I-20126 Milano, Italy.

[*]Corresponding author: Luca Menegon (luca.menegon@plymouth.ac.uk)

[†]Current address: Department of Computer Science, University of Warwick, United Kingdom.

[‡]Current address: Department of Earth, Ocean and Ecological Sciences, University of Liverpool, United Kingdom

Key Points:

- Multiple generations of pseudotachylytes and mylonites formed at 650-750 °C and 0.7-0.8 GPa in dry anorthosites from Lofoten (Norway)
- Strain localized in recrystallized pseudotachylytes deforming by diffusion creep
- Earthquakes are agents of weakening in the dry and strong lower crust

Abstract

The rheology and the conditions for viscous flow of the dry granulite facies lower crust are still poorly understood. Viscous shearing in the dry and strong lower crust commonly localizes in pseudotachylyte veins, but the deformation mechanisms responsible for the weakening and viscous shear localization in pseudotachylytes are yet to be explored. We investigated examples of pristine and mylonitized pseudotachylytes in anorthosites from Nusfjord (Lofoten, Norway). Mutual overprinting relationships indicate that pristine- and mylonitized pseudotachylytes are coeval and resulted from the cyclical interplay between brittle and viscous deformation. The stable mineral assemblage in the mylonitized pseudotachylytes consists of plagioclase, amphibole, clinopyroxene, quartz, biotite, ± garnet ± K-feldspar. Amphibole-plagioclase geothermobarometry and thermodynamic modelling indicate that pristine- and mylonitized pseudotachylytes formed at 650-750°C and 0.7-0.8 GPa. Thermodynamic modelling indicates that a limited amount of H_2O infiltration (0.20-0.40 wt%) was necessary to stabilize the mineral assemblage in the mylonite. Diffusion creep is identified as the main deformation mechanisms in the mylonitized pseudotachylytes based on the lack of crystallographic preferred orientation in plagioclase, the high degree of phase mixing, and the synkinematic nucleation of amphiboles in dilatant sites. Extrapolation of flow laws to natural conditions indicates that mylonitized pseudotachylytes are up to 3 orders of magnitude weaker than anorthosites deforming by dislocation creep, thus highlighting the fundamental role of lower crustal earthquakes as agents of weakening in strong granulites.

1 Introduction

Most of crustal seismicity is confined towards the base of the brittle upper crust at temperatures < 300°C [e.g. *Chen and Molnar*, 1983]. Interaction between lower crustal deformation and the earthquake cycle in the overlying seismogenic zone is observed as postseismic afterslip and interseismic creep in the lower crust [*Bodin and Horton*, 2004; *Wright et al.*, 2013]. However, the lower crust is also involved in earthquake nucleation [e.g., *Maggi et al.*, 2000; *Fagereng*, 2013], and this indicates a mechanically strong lower crust [*Maggi et al.*, 2000; *Jackson et al.*, 2004], at least transiently [*Handy and Brun*, 2004].

Important volumes of pseudotachylytes (generally interpreted as quenched melts caused by the frictional heat released during seismic slip) in exhumed lower crustal rocks, and formed at lower crustal conditions, have been taken as direct geological evidence for deep fracturing [*Austrheim and Blundy*, 1994; *Jackson et al.*, 2004; *Austrheim*, 2013]. Examples of deep fracturing is particularly common in dry rocks, and it is generally accepted that a strong, seismogenic lower crust requires anhydrous granulite facies material [*Jackson et al.*, 2004]. Anhydrous conditions in granulites inhibit crystal plastic flow and result in high strength [*Jackson et al.*, 2004; *Menegon et al.*, 2011]. Furthermore, anhydrous granulites can survive metastably in the course of Wilson cycles, unless they are infiltrated by fluids that trigger metamorphic reactions [*Austrheim*, 2013]. A picture is emerging in which a seismically active lower crust provides an environment for enhanced metamorphic and rheological transitions, due to fluid-rock interaction and associated reaction weakening in the fractured domains [*Austrheim*, 2013; *Austrheim et al.*, 2017]. The observation that viscous shearing in a dry and strong lower crust often localizes in pseudotachylyte veins [*Pennacchioni and Cesare*, 1997; *White*, 1996; 2012; *Steltenpohl et al.*, 2006; 2011; *Austrheim*, 2013; *Pittarello et al.*, 2013] is consistent with this picture. However, the deformation mechanisms responsible for the associated weakening

and viscous shear localization in pseudotachylyte veins are yet to be fully explored. Furthermore, whether lower crustal pseudotachylytes develop by fault-related frictional melting [*McKenzie and Brune*, 1972], by thermal runaway in ductile shear zones developing extreme localization and accelerated creep rates [*John et al.*, 2009], or by in-situ amorphization of crystalline material at high stresses and strain rates [*Pec et al.*, 2012] is still controversial.

Lofoten is one of the rare localities where the interplay between fracturing and viscous flow, and the processes leading to strain localization in dry, granulitic lower crust can be accurately studied, because (1) Lofoten exposes a relatively "intact" lower crust largely consisting of anhydrous granulites [*Corfu*, 2004], and (2) lower crustal shear zones in Lofoten are commonly associated with large volumes of pseudotachylytes [*Steltenpohl et al.*, 2006; 2011]. The study presented here investigates an exceptionally well preserved network of coeval lower crustal pseudotachylytes and mylonites from Lofoten, and discusses the conditions for pseudotachylytes development and the deformation mechanisms responsible of the ductile shear localization in pseudotachylyte veins.

2 Geological Setting

Lofoten islands in northern Norway consist of a NNE-SSW trending basement horst that is part of the Baltic Shield (Fig. 1a). Lofoten represents a tectonic window beneath the Caledonian orogen and is composed of an Archean to Paleoproterozoic metamorphic complex of para- and orthogneisses intruded, between 1870 and 1770 Myr, by a large Anorthosite-Mangerite-Charnockite-Granite (AMCG) suite [*Griffin et al.*, 1978; *Corfu*, 2004]. The AMCG suite consists of several plutons of anhydrous composition [*Markl et al.*, 1998; *Corfu*, 2004] emplaced into the granulitic crust at ambient conditions estimated at 750-800°C, and in the range between 0.4 and 1.0-1.2 GPa [*Markl et al.*, 1998, and references therein]. The primary igneous texture and the granulite facies mineral assemblage are generally well preserved.

Lofoten largely escaped the Caledonian tectono-metamorphic overprint, as result of water-deficient conditions that inhibited crystal plastic deformation and metamorphic re-equilibration of granulites [*Steltenpohl et al.*, 2004; *Leib et al.*, 2016; *Okudaira et al.*, 2017]. Despite the lack of a regional post-intrusive fabric, eclogite and upper amphibolite facies, localized shear zones are common in Lofoten [*Kullerud et al.*, 2001; *Steltenpohl et al.*, 2006, 2011; *Menegon et al.*, 2013]. Fracturing and pseudotachylyte formation have been reported to be key processes for shear zone initiation in Lofoten [*Steltenpohl et al.*, 2006; *Menegon et al.*, 2013, 2015], and available evidence indicates that the pseudotachylytes developed under lower crustal conditions [*Moecher and Steltenpohl*, 2009].

The Nusfjord eastern ridge in Flakstadøy (Fig. 1) exposes one of the largest bodies of anorthosites in Lofoten [*Markl et al.*, 1998]. The Nusfjord anorthosites are massive, coarse-grained rocks (1-5 cm average grain size of plagioclase) without any evident solid-state fabric. These rocks host a network of shear zones containing both pseudotachylytes and ultramylonites that are the main subject of this paper.

105 **3 Methods**

106 3.1 Microstructural observations and Electron Backscatter Diffraction (EBSD) analysis

107 Deformation microstructures and petrography were investigated using light and scanning
108 electron microscopy (SEM). Observations were made on polished thin sections cut perpendicular
109 to foliation and parallel to the stretching lineation (mylonites) and perpendicular to the
110 pseudotachylyte vein boundary. SEM analysis was performed at the Plymouth University
111 Electron Microscopy Centre using a JEOL LV6610 SEM and a JEOL 7001 FEG-SEM.

112 EBSD data were acquired on the JEOL LV6610 SEM equipped with a NordlysNano
113 EBSD detector (Oxford Instruments). Working conditions during acquisition of the EBSD
114 patterns were 20 kV, 70° sample tilt and high vacuum. EBSD patterns were acquired and
115 indexed with the AZtec software on rectangular grids with step size of 0.8 μm and 2.6 μm, and
116 processed with the Channel 5 software (Oxford Instruments).

117 3.2 Mineral chemistry

118 Major element mineral chemistry was measured with the JEOL 8200 Super Probe
119 electron micro-probe analyser (EMPA) at the Department of Earth Sciences, University of
120 Milan, Italy. Working conditions were 15 kV accelerating voltage, 5 nA current, 1 μm beam
121 diameter, using wavelength dispersive spectrometry (WDS) and natural silicates as standards.
122 All standards were calibrated within 0.5 % at one standard deviation and a PhiRhoZ routine was
123 used for matrix correction.

124 Mineral chemistry of amphibole-plagioclase pairs, used for the of P-T estimates, was
125 measured with the Cameca SX100 microprobe at the School of Earth Sciences, University of
126 Bristol, UK. Working conditions were 20 kV accelerating voltage, 5nA current, 1 μm beam
127 diameter, using wavelength dispersive spectrometry (WDS) and natural silicates as
128 standards.Fe^{3+} of amphiboles and garnets has been calculated from stoichiometry.

129 3.3 XRF analysis of bulk-rock chemical composition

130 Whole rock chemical analysis of major elements was performed by Wavelength
131 Dispersive X-Ray Fluorescence (WD-XRF) analysis with a Philips PW2400 equipped with a
132 rhodium tube at the Department of Geosciences, University of Padova, Italy. Powder samples
133 were mixed and diluted at 1:10 with $Li_2B_4O_7$ and $LiBO_2$ flux and melted into glass beads. Loss
134 on Ignition (LOI) was determined from weight lost after ignition at 860°C for 20 minutes and at
135 980°C for 2 hours. FeO was determined with permanganometry using a rhodium tube.

136 3.4 Thermodynamic modelling

137 H_2O-saturated P-T and T-H_2O isochemical sections were calculated with Perple_X
138 software [*Connolly*, 2005], in the system SiO_2-Al_2O_3-MgO-CaO-Na_2O-K_2O-TiO_2-FeO-(Fe_2O_3),
139 using the bulk composition of the mylonitized pseudotachylyte sample N13-10D and of the host
140 anorthosite sample N1310B (Table 1). We used the thermodynamic database and equation of
141 state for H_2O of *Holland and Powell* [1998, upgrade 2002] and no phase was excluded from the
142 calculation. We used the solution models of *Holland and Powell* [1998, 2003] for olivine,

orthopyroxene, clinopyroxene, garnet, spinel, phengite and feldspar, of *Tajcmanova et al.* [2009] for Ti-biotite, and of *Dale et al.* [2005] for calcic amphibole.

3.5 SIMS analysis

Intracrystalline hydrogen content in plagioclase was measured on polished thin sections using the Cameca ims-4f Secondary Ion Mass Spectrometry (SIMS) at the NERC Ion Microprobe Facility in Edinburgh, UK. Prior to analysis the sample was placed in an oven at 105°C for 30 minutes to remove surface humidity. The sample was then coated with a gold film (<0.02µm) and kept in the SIMS chamber under high vacuum (5×10^{-9} Torr) for > 48 hours. Analysis was performed with a 5nA primary beam of $^{16}O^-$ ions accelerated to 14.5 kV. To avoid surface contamination, few nm of surface material were removed by sputtering the spot for 4 minutes while rastering the beam (25 µm grid) before each measurement. Measurements were acquired using a beam spot size of 20 µm (±5 µm). Each analysis consisted of 20 cycles of the isotopes ^1H, ^{23}Na, ^{30}Si, ^{39}K and ^{49}Ti. For hydrogen only the last 15 cycles were averaged as ^1H signals stabilized only after the first cycles. Previously determined SiO_2 concentration was used as internal standard. Probing locations were identified beforehand and attention was paid to avoid cracks, grain-boundaries and alterations, which could contain free water. Basaltic glass standard St81A9 [*Lesne et al.*, 2011] was used to calibrate the water content in plagioclase. Anhydrous olivine standard (Kilbourne Hole) was used to correct for background ^1H signals (estimated at 12 wt ppm H_2O).

4 Field observations

The eastern ridge of Nusfjord peninsula is dominated by coarse-grained anorthosites with minor troctolites and gabbros. Satellite images show a network of 3 main sets of lineaments trending ENE-WSW to NE-SW (*Set 1*), NW-SE (*Set 2*), and NNE-SSW (*Set 3*) (Figs. 1b-c). In the field, the lineaments correspond to major (of as much as a few meters wide), steeply dipping mylonitic shear zones associated with sub-parallel 2nd order (cm-dm thick) discrete shear zones in between (Fig. 2). All three sets contain associations of pseudotachylytes and mylonites. The study presented here focuses on the *Set 1* shear zones, because it contains the largest volumes of pseudotachylytes in the area.

Set 1 shear zones dip steeply mostly towards the SE and contain a moderately to steeply plunging stretching lineation (Fig. 1c). The shear zones show normal-oblique kinematics, with a top-to-S component. The simplest type of 2nd order shear zone consists of a thin sharply bounded, homogeneously fine-grained (Figs. 2a-c), dark green sheared layer. This layer is typically surrounded by a < 10 cm wide bleached halo (contrasting in colour with the dark host anorthosite), which was partly involved in shearing (Figs. 2a-c). The bleached halo results from a pervasive network of white-coloured layers forming transgranular micro-fractures or exploiting the cleavage of the coarse anorthosite plagioclase (Fig. 2c).

The dark layers are homogeneously fine grained, regardless of the accommodated strain (Fig. 2d), indicating that the fine grain size did not result from progressive grain size refinement, but was a pristine feature of the shear zone precursor. These layers are identified as sheared

pseudotachylyte fault veins as indicated by the local preservation of pseudotachylyte breccia pockets (Fig. 2e) and injection veins (Fig. 2f-g), and by the local occurrence of undeformed pseudotachylytes trending parallel to the shear zones (Fig. 2h).

Thick shear zones have commonly a domainal foliation defined by elongated, alternating domains of whitish and dark-green colour (Fig. 3a-b). These latter domains are fine grained and similar to the deformed pseudotachylytes of the 2nd order shear zones; locally they are discordant to the main foliation (Fig. 3a). There is no compositional heterogeneity in the pristine anorthosite to explain the origin of such compositional banding of mylonitic rocks. The dark domains tend to anastomose around the white domains that represent stretched portions of the bleached/damaged host anorthosite. With increasing strain both types of domains tend to form a more regular, planar layering and macroscopic plagioclase porphyroclasts disappear. Large, low strain domains associated with some major shear zones locally show thick (20-50 cm) pseudotachylyte breccias with cm-sized lithic clasts of bleached anorthosite and clast-free layers of pseudotachylyte (Fig. 3c), parallel to the shear zone boundary. The origin of the sheared dark domains from pseudotachylytes is indicated by the common occurrence of undeformed pseudotachylyte injection veins in the anorthosite wall rock of shear zones.

In some cases, the pseudotachylyte veins crosscut the mylonitic foliation. In Fig. 3d, the foliation of a shear zone, that includes sheared pseudotachylytes, is involved in a breccia cemented by a pseudotachylyte that exploited the shear zone boundary. Fig. 3e shows a pseudotachylyte-bearing fault sharply displacing a localized ductile shear zone and being in turn dragged into a ductile shear zone that exploits older pseudotachylyte veins (Fig. 3f).

5 Microstructure

5.1 Anorthosite host rock

Anorthosite consists of large (as much as 20 cm in size) plagioclase crystals and subordinate (< 10%) clinopyroxene, orthopyroxene and olivine.(Fig 4a). Clinopyroxene is the most common mafic phase. Hydrous phases are very rare (< 1 %) and consist of local biotite rims around orthopyroxene and of discontinuous amphibole coronas around clinopyroxene . Corundum locally occurs as idiomorphic single crystals or as aggregates included in mm-sized magnetite. A detailed description of the Nusfjord anorthosites is reported in *Markl et al.* [1998].

5.2 Pseudotachylyte and associate damage zone

Pseudotachylytes locally preserve the pristine microstructure that includes microlites of plagioclase, clinopyroxene, amphibole and orthopyroxene (Figs. 4a-c), flow structures, and chilled margins (Fig. 4d). Pristine pseudotachylytes consist of single-generation individual veins with no evidence of multiple veins along the same fault.

The pseudotachylyte matrix is microcrystalline and dominantly consists of very fine-grained (< 5 μm) plagioclase. Plagioclase, and rarer clinopyroxene and orthopyroxene, occur as clasts in the pseudotachylyte matrix together with lithic clasts. The shape of clasts ranges from angular to smoother shapes showing resorption structures. In the damage zone flanking

pseudotachylyte, plagioclase and clinopyroxene show undulatory extinction, bent twins and bent lamellae (in pyroxenes). The grains show fractures filled with new small polygonal grains (20-30 μm in size) forming bands up to 100 μm wide (Fig. 4a). In clinopyroxene the intracrystalline bands of new grains locally contain minor amounts of amphibole.

Some pseudotachylytes have completely lost the pristine microlitic microstructure and have recrystallized into a fine-grained (average grain size ~ 10 μm) mixture of plagioclase, amphibole, clinopyroxene, biotite, quartz ± K-feldspar ± orthopyroxene ± ilmenite (Fig. 4e). Since these pseudotachylytes do not show a mylonitic overprint, we refer to them as to *recrystallized pseudotachylytes*.

Garnet is common in pristine and recrystallized pseudotachylytes as well as in the wall rock anorthosite. In pristine pseudotachylytes, garnet occurs as small (50-100 μm) euhedral grains arranged as: (i) overgrowths on plagioclase clasts (Fig. 4b); (ii) framboidal rims around opaque grains; (iii) trails along thin healed microcracks confined within the pseudotachylyte vein; and (iv) trails along the pseudotachylyte boundary.

5.3 Ductile shear zones

Mylonitized pseudotachylytes consist of a fine-grained (average grain size: 5-30 μm) mixture of plagioclase, amphibole and clinopyroxene, with less abundant garnet, biotite, quartz, K-feldspar and ilmenite (Fig. 5b). Amphibole is typically found as isolated grains and small clusters (< 50 μm in length) at triple junctions between plagioclase grains (Fig. 5b), as well as along C' shear bands. The amount of amphibole in the phase mixture, estimated with image analysis on SEM backscatter electron images, is in the range of 5-10 vol%. Garnet is present as isolated grains (typically < 20 μm in size) dispersed in the phase mixture, and as polycrystalline clusters where individual grains are up to 200 μm in size (Fig. S1). Most of the garnets contain inclusions of plagioclase, clinopyroxene and amphibole. Isolated grains of garnet are typically inclusion-free.

Mylonitic pseudotachylytes wrap around lenses deriving from the grain size reduction of original plagioclase and clinopyroxene of the anorthosites. In these lenses, plagioclase is variably fractured and recrystallized to fine-grained (average grain size of 25 μm) mono-mineralic aggregates elongated parallel to the shear zone foliation. The relict porphyroclasts show undulatory extinction and bent twins (Figs. 5a, 5c). Clinopyroxene porphyroclasts are partially to completely replaced by fine-grained (< 30 μm) clinopyroxene, amphibole and quartz neoblasts along intracrystalline bands and along the boundaries with plagioclase (Fig. 5d). The clinopyroxene-derived aggregates are also stretched parallel to the mylonitic foliation (Fig. 5c).

Plagioclase and clinopyroxene in the damage zone flanking the ductile shear zones are pervasively fractured and show undulatory extinction. Fractures are filled with new small polygonal grains of plagioclase (within plagioclase) and clinopyroxene + amphibole ± quartz (within clinopyroxene). The new grains are 5-30 μm in size and form up to 200 μm wide

intracrystalline bands (Fig. 5e). These microstructures are identical to those of the damage zone flanking pristine pseudotachylyte veins.

6 EBSD analysis

The crystallographic preferred orientation (CPO) of plagioclase determined by EBSD in the polyphase matrix of the mylonitic pseudotachylyte (Fig. 6a) does not show an obvious alignment of lattice planes and axes with the foliation and with the stretching lineation, respectively (Fig. 6b). On the contrary, amphibole has a CPO of the (100) planes distributed along a discontinuous girdle subparallel to the YZ plane of the finite strain ellipsoid, with a maximum near the pole to the foliation (Fig. 6b). The [001] axis forms a maximum on the foliation plane at a low angle to the stretching lineation.

The misorientation axis distribution (MAD) of random pairs of both plagioclase and amphibole is remarkably close to the theoretical curve for a random distribution (Fig. 6c). Correlated pairs of both plagioclase and amphibole show that misorientations $< 50°$ occur with a higher frequency than for a random distribution (Fig. 6c).

The long axes of amphibole grains are preferentially oriented at an angle of 5-20° measured counter-clockwise from the trace of the ultramylonite foliation (Fig. 6d). For the sinistral sense of shear of the ultramylonite in Fig. 7a, the preferred orientation of the long axes of amphibole corresponds to a C′-type shear band orientation.

Recrystallized plagioclase in an elongated mono-mineralic aggregate embedded in mylonitized pseudotachylytes (Fig. 7a) shows a grain size range from 4 μm to about 120 μm (Fig. 7b). Grains larger than 30 μm are preferentially oriented with the (001) planes subparallel to the foliation and with the [110] direction subparallel to the stretching lineation. Grains smaller than 30 μm show a remarkable dispersion of the crystallographic planes and axes, but many small grains overlap in orientation with the larger grains (Fig. 7c). Misorientations $< 70°$ occur with a higher frequency than for a theoretical random distribution for both correlated and uncorrelated pairs (Fig. 7d). The misorientation axis for low misorientations (3-10°) is preferentially parallel to the [-100] axis (Fig. 7d).

7 Mineral chemistry and P-T-H_2O conditions of deformation

The major element compositions of representative minerals in pristine, recrystallized, and mylonitized pseudotachylytes are reported in Tables S1-S3 in the supplementary material. Plagioclase of the host rock has ~77 mol% of anorthite component (bytownite). Plagioclase microlites and recrystallized plagioclase (both in recrystallized and in mylonitized pseudotachylytes) have lower anorthite contents, mostly in the range between 46 and 52 mol%

(andesine), but with a few recrystallized grains containing up to 58 mol% of anorthite (Table S1).

Clinopyroxene is diopside, with similar Al contents of 0.15-0.20 atoms per formula unit (a.p.f.u.) in both the host rock and in the recrystallized grains in the mylonite (Table S2). X_{Mg} values ($Mg/(Mg+Fe^{2+})$) range from 0.76 to 0.84, with the highest values found in clinopyroxene inclusions in garnet (table S2). Orthopyroxenes occur in the host rock, as survivor clasts and as microlites in the pseudotachylytes, and as porphyroclasts in the mylonites. They have similar compositions with X_{Mg} of ~0.57–0.68 and Al contents from 0.10 to 0.14 a.p.f.u., and up to 0.20 a.p.f.u. in the microlites (Table S2).

Amphiboles are pargasites and have Ca ~1.90, $(Na+K)_A$ from 0.71 to 0.85 and Si ranging from 5.98 to 6.35 a.p.f.u. (Table S3). The values of X_{Mg} range from 0.55 to 0.63, up to 0.68 for those included in garnet in the mylonites. Amphiboles do not show any variation of $(Na+K)_A$ and $Al^{(VI)}$ indicative of edenite substitution. The almost homogeneous composition of amphiboles in the various microstructural sites of pristine, recrystallized and mylonitized pseudotachylytes suggests similar equilibrium conditions during the formation, recrystallization, and shearing of pseudotachylytes.

Table S3 also shows the compositions of garnets overgrowing plagioclase survivor clasts in pseudotachylytes, in coronas around corundum in the host rock, and in the mylonitized pseudotachylytes. All garnets have the same almandine content (~50 mol%), except those around corundum (59 mol%). They instead record variable grossular and pyrope contents with values ranging from 28 to 39 mol% of grossular, corresponding to a variation from 24 to 11 mol% of pyrope (Table S3).

Tables S1 and S3 also report representative compositions of plagioclase and amphibole pairs used for conventional geothermobarometry calculations. Temperature was estimated with the thermometer of *Holland and Blundy* [1994], which considers the exchange reaction edenite + albite = richterite + anorthite and was calibrated in the P, T range of 0.1-1.5 GPa and 400-1000 °C. Pressure was estimated with the barometer of *Anderson and Smith* [1995], which is based on the increase of Al content in hornblende with increasing P and was calibrated in the T range between 675 and 760 °C. The resulting P, T conditions of sin-kinematic recrystallization in the mylonitized pseudotachylytes are estimated at 700-750°C, 0.7-0.9 GPa.

These results are in agreement with the P-T stability field modelled in Figure 8a for H_2O-saturated conditions, which were chosen because we interpret the syn-kinematic nucleation of amphibole at triple junctions as the evidence of the presence of H_2O at grain boundaries. The mineral assemblage consisting of biotite – amphibole – plagioclase – clinopyroxene – quartz – ilmenite found along the recrystallized and mylonitized pseudotachylytes (Figs. 4e, 5b) is stable in the red P-T area of Fig. 8a, at around 650 °C and 0.7 GPa. Syn- to post-kinematic garnet extends the stability field up to 750 °C and 0.85 GPa. These maximum temperatures correspond to the stability limit of amphibole for the studied composition. Below 750 °C, the stability of amphibole is also governed by the amount of water assisting the deformation, as portrayed in the T-X(H_2O wt%) section of Figure 8b, calculated at 0.7 GPa. At least 0.25 wt% of H_2O is required to crystallise amphibole and 0.5 wt% to saturate the system in the temperature range from 575 to 750 °C. For higher H_2O contents, the modal amount of amphibole is only dependent on the

equilibration temperature, as shown by the grey lines that indicate the locus of points of equal amount (vol%) of amphibole for the various modelled mineral assemblages.

To evaluate if fluid infiltration was required in order to stabilize the mineral assemblage of the mylonitzed pseudotachylytes, we modelled the variation of modal abundances of mineral phases in the pristine anorthosites as a function of the H_2O content. The calculations have been performed at the estimated P, T conditions of deformation (700° C and 0.7 GPa) and the results are shown in Fig. 9. The diagram shows that < 1 vol% of biotite requires approximately 0.04 wt% of H_2O, and that such a low amount of H_2O would not result in the presence of free intergranular H_2O in the anorthosite protolith at the estimated P, T conditions of deformation. Thus, the amount of fluid present in the anorthosite is about six to ten times less than that required to stabilize the mineral assemblage of the mylonitized pseudotachylytes.

8 Intracrystalline water content in plagioclase

Brittle fracturing can introduce fluids into grain interiors even at high P-T conditions and this typically favours hydrolytic weakening [e.g. *Stünitz et al.*, 2017]. The measurement of the intracrystalline water content in plagioclase was carried out to test if fracturing and pseudotachylyte formation was accompanied by fluid infiltration in the interior of the grains. We measured the intracrystalline H content in plagioclase grains along 1.5 cm long transects from the undeformed anorthosite to the pristine pseudotachylyte, where the measurements were restricted to survivor clasts.

Most of the measurements indicate intracrystalline water contents < 40 ppm both in the anorthosites and in survivor clasts in the pseudotachylyte (Fig. 10). There is no progressive increase of water concentration in plagioclase towards the pseudotachylyte vein, and many clasts inside the veins and at the pseudotachylyte vein boundary have water concentration < 20 ppm. There are few grains with intracrystalline water content > 70 ppm both in the host rock and in the pseudotachylyte. SEM inspection of the probe pits indicates that these higher water concentrations occur in close proximity to lamellae of K-feldspar, presumably resulting from exsolution of original ternary feldspars (Fig. S2).

9 Discussion

9.1 Cyclic interplay between brittle and viscous deformation at lower crustal conditions

Field observations in Nusfjord indicate that ductile shear zones exploited a set of pseudotachylyte-bearing faults. This is consistent with the general observation that nucleation of ductile shear zones requires the presence of a planar compositional or structural precursor [e.g. *Pennacchioni and Mancktelow*, 2007; *Pennacchioni and Zucchi*, 2013]. In Nusfjord, pseudotachylytes provided both the structural anisotropy of long, sub-parallel fault planes and the compositional precursor of weak, fine-grained pseudotachylyte fault veins decorating the slip surfaces. The alternation of thinner and thicker shear zones apparently reflects the original hierarchical organization of the precursor pseudotachylyte-bearing faults [*Pennacchioni*, 2005;

375 *Di Toro and Pennacchioni*, 2005]. Thin shear zones derive from single mm-cm thick
376 pseudotachylyte fault veins that only locally include pockets of pseudotachylyte breccias. Major
377 shear zones overprinted complex bands of more pervasive pseudotachylyte veining and
378 brecciation.

379 The mutual overprinting relationships between pristine and mylonitized pseudotachylytes
380 (Figs. 3d-f) are interpreted to result from the cyclic interplay between brittle and viscous
381 deformation. Thus, the P-T conditions of deformation estimated for the mylonitized
382 pseudotachylytes are considered representative also of the conditions of formation of
383 pseudotachylytes. This is supported by the similarity in microstructure of the damage zone
384 flanking both pristine and mylonitized pseudotachylytes showing neoblasts of clinopyroxene and
385 amphibole, and the lack of low-grade minerals (Figs. 4a, 5e).

386 The P-T conditions of deformation are constrained at 650-750°C and 0.7-0.8 GPa
387 (depending on the stability of garnet), using both amphibole-plagioclase conventional
388 geothermobarometry and thermodynamic forward modelling. Assuming an average crustal rock
389 density of 2700-3000 kg/m^3, these conditions correspond to a depth range of 24-30 Km and
390 indicate a lower crustal setting for the brittle-viscous deformation cycles.

391 9.2 Origin of pseudotachylytes at lower crustal conditions

392 Generation of pseudotachylytes at depths below the classic (10-15 km depth) brittle-ductile
393 transition in the continental crust has been interpreted to result from different processes: (1)
394 frictional melting during seismic slip, either due to the downward propagation of seismic
395 ruptures nucleated in the upper brittle crust [e.g. *Ellis and Stöckhert*, 2004; *Lin et al.*, 2005;
396 *Moecher and Steltenpohl*, 2011] or to the nucleation of lower crustal earthquakes [*Jackson et al.*,
397 2004; *Austrheim*, *2013*; *Austrheim et al.*, 2017], (2) plastic instabilities [*Hobbs et al.*, 1986;
398 *White*, 1996, 2012], (3) self-localizing thermal runaway [e.g. *John et al.*, 2009; *Andersen et al.*,
399 2014], (4) in-situ amorphization during high stress deformation at slow displacement rates [*Pec*
400 *et al.*, 2012]. Plastic instabilities and self-localizing thermal runaway require a ductile precursor
401 of a pseudotachylyte-bearing fault. In these models, seismic slip localization and melting result
402 from the feedback between shear heating and thermal softening within a ductile shear zone.
403 However, pseudotachylytes by themselves cannot be taken as unequivocal field evidence for
404 thermal runaway processes, unless they contain clasts of mylonites that could suggest the
405 presence of a ductile precursor. The plastic instability and thermal runaway models do not seem
406 appropriate for the Nusfjord case, because a large amount of pseudotachylytes clearly predates
407 the mylonitic deformation (e.g. Figs. 2f, 3f). The pristine pseudotachylytes contain in most of the
408 cases abundant survivor clasts and lithic clasts of the host shattered anorthosite, but not of
409 mylonites (Fig. 4a). In-situ amorphization is difficult to reconcile with the extensive occurrence
410 of microlites (Figs. 4b, 4c), with the formation of chilled margins (Figs. 2g, 4d) and with the
411 large volumes of pseudotachylytes. Thus, we interpret the Nusfjord pseudotachylytes as the
412 result of frictional melting on fault planes during seismic slip in the lower crust.

413 Generation of pseudotachylytes by brittle deformation at lower crustal conditions has been
414 explained by local high fluid pressure promoting fracturing [e.g. *Lund and Austrheim*, 2003;
415 *Steltenpohl et al.*, 2006]. However, the Nusfjord pseudotachylytes are not spatially associated
416 with any vein system, and there is no evidence of hydration of the pseudotachylytes with respect

to their host rock (Table 1, Fig. 8, and see section 9.3). This is consistent with the development of the Nusfjord pseudotachylytes as the product of co-seismic brittle deformation of effectively dry rocks devoid of an intergranular pore fluid. The absence of free aqueous fluid in interconnected intergranular pore space inhibits viscous deformation and results in a high strength of lower crustal rocks [*Fitz Gerald et al.*, 2006; *Menegon et al.*, 2011]. In the absence of elevated pore fluid pressure, high differential stresses are necessary to fracture dry lower crustal rocks. Thus, we interpret the widespread occurrence of pseudotachylytes generated by co-seismic brittle deformation in Nusfjord as the evidence of a strong, seismogenic lower crust with a rheology equivalent to that of anhydrous granulite facies material [*Maggi et al.*, 2000; *Jackson et al.*, 2004]. Crustal strength calculations suggest that deep seismicity at depths greater than 30 km in the Rukwa-Malawi rift zone is best explained by the rheology of a mafic granulitic lower crust [*Fagereng*, 2013]. Likewise, an analysis of the aftershocks following the 2001 M_w 7.6 Bhuj earthquake revealed that they were indeed located mostly in the lower crust at a depth of about 26 km, and this was explained invoking a mafic granulite rheology of the deeper crustal levels [*Bodin and Horton*, 2004]. Thus, we conclude that the lower crustal Nusfjord earthquakes are consistent with the nucleation of seismic ruptures at depth > 25 km, or with a downward propagation of seismic ruptures from the deep brittle-ductile transition in dry anorthosites, and not from the typical shallower transition in the upper continental crust.

9.3 Deformation mechanisms in the mylonitized pseudotachylytes and the role of fluids

Monomineralic plagioclase layers embedded in mylonitized pseudotachylytes show a moderate CPO consistent with dislocation creep by ½ (001) [110] slip system (Fig. 7c) [e.g. *Kruse et al.*, 2001]. Deformation by dislocation creep in plagioclase monomineralic layers is suggested by the overlap in crystallographic orientation between porphyroclasts and recrystallized grains (Fig. 7c), by the excess of low angle boundaries (< 20°, Fig. 7d), and by the clusters of misorientation axes parallel to crystallographic axes for low misorientations (3-10°, Fig. 7d). Many recrystallized grains show a significant dispersion of crystallographic orientations from the one of the host porphyroclasts (Fig. 7c). This is consistent with a contribution of grain boundary sliding after the recrystallization of plagioclase. However, monomineralic layers are typically wrapped by recrystallized pseudotachylytes, and this suggests that the polyphase mixture deriving from recrystallization of pseudotachylytes is rheologically weaker than monomineralic plagioclase domains deforming by dislocation creep.

The fine grain size of the phase mixture (5-30 μm) and the high degree of phase mixing suggest that mylonitized pseudotachylyte deformed by diffusion creep and grain boundary sliding. The plagioclase weak CPO is not consistent with dislocation creep along common slip systems (Fig. 6b). Amphibole has a clear CPO of the (100) planes and [001] direction, but the same CPO has been observed in amphibolites deformed experimentally in the diffusion creep regime [*Getsinger and Hirth*, 2014]. We interpret the amphibole CPO as the result of oriented grain growth and rigid body rotation during diffusion creep, as concluded for other natural samples deformed at lower crustal condition [e.g. *Berger and Stünitz*, 1996; *Getsinger et al.*, 2013; *Menegon et al.*, 2015; *Okudaira et al.*, 2015]. Thus, we conclude that the brittle grain size reduction due to pseudotachylyte formation, the fine grain size, and the polymineralic composition (inhibiting grain growth) of pristine- and recrystallized pseudotachylytes (Figs. 4c, 4e) predisposed pseudotachylytes veins and the surrounding damage zone to subsequent strain localization by grain size sensitive creep. A similar origin of ultramylonites deforming by grain

size sensitive creep was proposed by *White* [1996], who identified the recrystallization of precursor pseudotachylyte veins as the key grain-size reduction mechanism necessary to produce ultramylonites.

Strain localization triggered by lower crustal seismicity has typically been associated with fluid infiltration and associated reaction weakening in the fractured and hydrated domains [*Austrheim*, 2013, and references therein]. Our results indicate that the formation of mylonitized pseudotachylytes required a six- to ten-fold increase in H_2O content with respect to the anorthosite protolith (Figs. 8b and 9).

In the mylonitized pseudotachylytes, amphibole crystallisation in equilibrium with biotite, plagioclase, clinopyroxene, quartz, ilmenite, ± garnet occurred for H_2O contents above 0.25 wt% at P = 0.7 GPa and T up to 750 °C. At H_2O-undersaturated conditions, amphibole content is strongly dependent on the water content of the system. It is worth noting that at T = 700 °C, 0.45 wt% of water enabling the crystallisation of 8 vol% of amphibole (which represents the average amount of amphibole in the mylonitized pseudotachylytes as estimated with image analysis) is coincident with the limit of H_2O saturation. At higher temperatures, the limit is reached at even lower water contents. This means that very low H_2O is needed to stabilise the observed syn-deformation paragenesis and, more important, that 0.25-0.45 wt% of H_2O is sufficient to saturate the entire rock system at the P, T conditions of deformation. Thus, although H_2O infiltration is required to stabilize the mineral assemblage in the mylonitized pseudotachylytes, the amount of H_2O infiltration that resulted in rheological weakening is minimal. *Okudaira et al.* [2015] reported similar low values of water contents during diffusion creep deformation in gabbro ultramylonites following a precursor fracturing stage at granulite facies conditions.

This is consistent with experimental results of *Milke et al.* [2012], which showed that very little amounts of water present as a pore fluid are effective in facilitating mineral reactions if rock deformation maintains a sufficient porosity. Moreover, relatively low water contents (~0.07 wt%) are commonly referred to as wet conditions during experimental rock deformation of feldspar rocks in the viscous regime, and are sufficient to activate diffusion creep [*Rybacki and Dresen*, 2000; *Dimanov et al.*, 2005]. We argue that brittle grain size reduction followed by diffusion-accommodated viscous grain boundary sliding enhanced the porosity of the mylonitized pseudotachylytes, and resulted in the distribution of the infiltrated fluids along the grain boundaries. Diffusion-accommodated viscous grain boundary sliding can maintain a dynamic porosity in ultramylonites [*Fusseis et al.*, 2009], which can evolve into the development of creep cavitation bands decorated by new grains that precipitate from the grain boundary fluid [*Menegon et al.*, 2015]. In the Nusfjord mylonitized pseudotachylytes, the possible signature of creep cavitation bands is the preferred orientation of amphibole long axis parallel to a C′-type shear band orientation (Fig. 6d), similar to the microstructures described in *Menegon et al.* [2015]. The water redistributed along the grain boundaries made the system wet at the shear zone scale, and facilitated heterogeneous phase nucleation, as demonstrated by the syn-kinematic growth of amphiboles at triple junctions and dilatant sites (Figs. 5b, 6a). This stabilized strain localization in the polymineralic, fine-grained mylonitized pseudotachylytes. Therefore, it is the

water at grain boundaries that has a major rheological effect on lower crustal shear zones, by facilitating diffusion creep deformation and phase nucleation.

Measurements of intracrystalline water content of plagioclase do not show a systematic increase from the host rock to the pseudotachylytes. This lends further support to our interpretation that the infiltrated aqueous fluid was redistributed along the grain boundaries rather than penetrating the interior of nominally anhydrous minerals via (micro)cracking. The low intracrystalline water contents in plagioclase (Fig. 10) were apparently sufficient for limited dislocation creep to occur (Fig. 7). However, this did not result in the nucleation of ductile shear zones in intact anorthosites, which instead required a precursor stage of co-seismic brittle deformation with associated fluid redistribution at the grain boundaries.

9.4 Rheology of mylonitized pseudotachylytes

To evaluate the extent of weakening resulting from diffusion creep in the mylonitized pseudotachylytes, we compared the rheology of plagioclase deforming by dislocation creep with the rheology of a plagioclase + clinopyroxene aggregate deforming by diffusion creep. The general flow law for dislocation creep is:

$$\dot{\varepsilon} = A\sigma^n \exp(-Q/RT) \qquad (1)$$

where $\dot{\varepsilon}$ is the strain rate, A an empirical constant, σ the differential stress, n the stress exponent, Q the activation energy, R the gas constant, and T the temperature. We used the flow laws for dislocation creep of wet and dry anorthite of *Rybacki and Dresen* [2000]. Dry conditions were chosen to predict the rheology of the anorthosite host rock deforming by dislocation creep and devoid of an intergranular pore fluid phase, whereas wet conditions were chosen to simulate the rheology of monomineralic plagioclase layers embedded in mylonitized pseudotachylytes, which deformed in the presence of H_2O (Figs. 4b, 8).

Deformation accommodated by diffusion creep is described by the flow law:

$$\dot{\varepsilon} = A\sigma^n d^m \exp(-Q/RT) \qquad (2)$$

where d is the grain size and m the grain size exponent. We use the flow law for diffusion creep of anorthite + diopside aggregates of *Dimanov and Dresen* [2005]. This flow law was chosen because (1) it approximates the composition of the mylonitized pseudotachylytes, and (2) it was derived for grain boundary diffusion-controlled creep, which is consistent with the deformation mechanisms identified in the mylonitized pseudotachylytes. We considered the flow

law for wet diffusion creep of an aggregate consisting of 75% anorthite (average grain size of ca. 3.5 μm) and 25% diopside (grain size < 35 μm) [*Dimanov and Dresen*, 2005].

Rheological calculations show that at T = 700° C the differential stress required to sustain geologically realistic strain rates of 10^{-10}–10^{-13} s^{-1} in the anorthite + diopside aggregate deforming by diffusion creep would be 1–3 orders of magnitude smaller than the stress required to deform plagioclase by wet dislocation creep, and up to 5 orders of magnitude smaller than then stress required to deform plagioclase by dry dislocation creep (Fig. 11). Furthermore, in the differential stress range between 10 and 0.1 MPa, deformation by diffusion creep in the anorthite – diopside aggregate would occur 3-7 orders of magnitude faster than deformation by dislocation creep in wet plagioclase. Thus, the weakening from activation of diffusion creep in the fine-grained polyphase mixture derived from recrystallization of pseudotachylytes is predicted to be significant. Similar effects of grain size reduction, marked weakening, and enhanced creep rates through activation of diffusion creep in recrystallized pseudotachylytes have been proposed by *White* [1996].

10 Conclusions

In the dry anorthosites from Nusfjord (Lofoten, northern Norway) different generations of pseudotachylytes and mylonites formed at lower crustal conditions of 650-750 °C and 0.7-0.9 GPa, as estimated with conventional geothermobarometry and with thermodynamic forward modelling. Mylonites exploited pristine pseudotachylytes veins, which provided both a structural and a compositional precursor for the nucleation of ductile shear zones.

Pristine and mylonitized pseudotachylytes show mutual overprinting relationships that are interpreted as the result of the cyclic interplay between brittle and viscous deformation at lower crustal condition. Pseudotachylytes formed by brittle co-seismic deformation in relatively dry and strong anorthosites, as the result of seismic ruptures nucleated in the deep crust or of the downward propagation of seismic ruptures from the deep brittle-ductile transition in dry anorthosites.

Strain localization in mylonitized pseudotachylytes was facilitated by the grain size reduction due to the formation and subsequent recrystallization of pseudotachylytes to a fine-grained (< 30 μm) polyphase aggregate. Microstructural observations and EBSD analysis are consistent with diffusion creep as the dominant deformation mechanism in the mylonitized pseudotachylytes. Thermodynamic modelling combined with microstructural observations indicate that the fluid infiltration necessary to stabilize the mineral assemblage of the mylonitized pseudotachylytes was minimal, on the order of 0.20-0.40 wt% H_2O. The infiltrated aqueous fluid was redistributed along the grain boundaries in the fractured domains, and made the system wet and weak at the shear zone scale. Diffusion-accommodated viscous grain boundary sliding maintained a dynamic porosity in the mylonitized pseudotachylytes, and

produced creep cavitation and precipitation of material from grain boundary fluids collected in creep cavities and in other dilatant sites.

Extrapolation of experimentally derived flow laws to geologically realistic strain rates at a temperature of 700°C indicates up to 3 orders of magnitude weakening in the mylonitized pseudotachylytes deforming by diffusion creep with respect to plagioclase deforming by dislocation creep in the anorthosite host rock. This highlights that pseudotachylytes caused by brittle faulting can be precursors of viscous, weak shear zones in the dry lower crust, indicating lower crustal earthquakes as agents of rheological change from strong, brittle crust, to strong crust with embedded fine grained, weak viscous shear zones.

Acknowledgments

This study has been funded by a FP7 Marie Curie Career Integration Grant to L.M. (grant agreement PCIG13-GA-2013-618289) and by two Plymouth University MGeol bursaries to K.H. and E.W. We gratefully acknowledge the constructive reviews of John Platt, Takamoto Okudaira and Johann Diener, and the editorial handling of Thorsten Becker. We would like to thank Neil Mancktelow, Joseph Clancy White, Holger Stünitz, Petr Jeřábek, Luiz Morales, Erik Rybacki, Tim Redfield, Mark Anderson and Giulio Viola for all the stimulating discussions on this work. The staff at Plymouth University Electron Microscopy Centre is thanked for their support during SEM-based analyses. Cees-Jan De Hoog and the staff at the NERC Ion Microprobe Facility in Edinburgh are thanked for their support during SIMS analysis. Supplementary data supporting this work is available as online supporting information. Any other data can be requested to the corresponding author by email.

References

Andersen, T. B., H. Austrheim, N. Deseta, P. Silkoset, and L. D. Ashwal (2014), Large subduction earthquakes along the fossil Moho in Alpine Corsica, Geology 42, 395-398, doi:10.1130/G35345.1

Anderson, J. L., and D. R. Smith (1995), The effects of temperature and fO_2 on the Al-in-hornblende barometer, American Mineralogist 80, 549-559.

Austrheim, H. (2013), Fluid and deformation induced metamorphic processes around Moho beneath continent collision zones: Examples from the exposed root zone of the Caledonian mountain belt, W-Norway, Tectonophysics 609, 620-635.

Austrheim, H., and T. M. Blundy (1994), Pseudotachylytes generated during seismic faulting and eclogitization of the deep crust, Science 265, 82-83.

Austrheim, H., K. G. Dunkel, O. Plümper, B. Ildefonse, Y. Liu, and B. Jamtveit (2017), Fragmentation of wall rock garnets during deep crustal earthquakes, Science Advances 3, e1602067.

Berger, A., and H. Stünitz (1996), Deformation mechanisms and reaction of hornblende: Examples from the Bergell Tonalite (Central Alps), Tectonophysics 257, 149-174.

Bodin, P., and S. Horton (2004), Source Parameters and Tectonic Implications of Aftershocks of the M_w 7.6 Bhuj Earthquake of 26 January 2001, Bulletin of the Seismological Society of America 94, 818-827.

Chen, W.-P., and P. Molnar (1983), Focal depths of intracontinental and intraplate earthquakes and their implications for the thermal and mechanical properties of the lithosphere, Journal of Geophysical Research 88, 4183-4214.

Connolly, J. A. D. (2005), Multivariable phase diagrams: an algorithm based on generalized thermodynamics, American Journal of Science 290, 666–718.

Corfu, F. (2004), U–Pb Age, Setting and Tectonic Significance of the Anorthosite–Mangerite–Charnockite– Granite Suite, Lofoten–Vesterålen, Norway, Journal of Petrology 45, 1799-1819.

Dale, J., R. Powell, R. W. White, F. L. Elmer, and T. J. B. Holland (2005), A thermodynamic model for Ca-Na clinoamphiboles in Na2O-CaO-FeO-MgO- Al2O3-SiO2-H2O-O for petrological calculations, Journal of Metamorphic Geology 23, 771–91.

Dimanov, A., and G. Dresen (2005), Rheology of synthetic anorthite-diopside aggregates: Implications for ductile shear zones, Journal of Geophysical Research 110, B07203, doi:10.1029/2004JB003431.

Di Toro, G., and G. Pennacchioni (2005), Fault plane processes and mesoscopic structure of a strong-type seismogenic fault in tonalities (Adamello batholith, Southern Alps, Tectonophysics 402, 55-80, doi: 10.1016/j.tecto.2004.12.036

Ellis, S., and B. Stöckhert (20040, Elevated stresses and creep rates beneath the brittle-ductile transition caused by seismic faulting in the upper crust, Journal of Geophysical Research – Solid Earth 109, B05407 1-10.

Fagereng, Å. (2013), Fault segmentation, deep rift earthquakes and crustal rheology: Insights from the 2009 Karonga sequence and seismicity in the Rukwa–Malawi rift zone, Tectonophysics 601, 216-225.

Fitz Gerald, J. D., N. S. Mancktelow, G. Pennacchioni, and K. Kunze, K. (2006), Ultrafine-grained quartz mylonites from high-grade shear zones: Evidence for strong and dry middle to lower crust, Geology, 34, 369-372.

Fusseis, F., K. Regenaure-Lieb, J. Liu, R. M. Hough, and F. De Carlo (2009), Creep cavitation can establish a dynamic granular fluid pump in ductile shear zones, Nature 459, 974–977, doi:10.1038/nature08051.

Getsinger, A. J., and G. Hirth, (2014), Amphibole fabric formation during diffusion creep and the rheology of shear zones, Geology 42, 535-538.

Getsinger, A. J., G. Hirth, H. Stünitz, and E. T. Goergen (2013), Influence of water on rheology and strain localization in the lower continental crust, Geochemistry, Geophysics, Geosystems 14, 2247–2264, doi:10.1002/ggge.20148.

Griffin, W. L., P. N. Taylor, J. W. Hakkinen, K. S. Heier, I. K. Iden, E. J. Krogh, O. Malm, K. I. Olsen, D. E. Ormaasen, and E. Tveten (1978), Archaean and Proterozoic crustal evolution in Lofoten-Vesterålen, N Norway, Journal of the Geological Society of London 135, 629-647.

651 Handy, M. R., and J.-P. Brun (20040, Seismicity, structure and strength of the continental
652 lithosphere, Earth and Planetary Science Letters 223, 427-441.

653 Hobbs, B. E., A. Ord, and C. Teyssier (1986), Earthquakes in the Ductile Regime?, Pure and
654 Applied Geophysics 124, 309-336.

655 Holland, T., and J. Blundy (1994), Non-ideal interactions in calcic amphiboles and their bearing
656 on amphibole-plagioclase thermometry, Contributions to Mineralogy and Petrology, 116,
657 433-447.

658 Holland, T. J. B., and R. Powell (1998), An internally con- sistent thermodynamic data set for
659 phases of petro- logic interest, Journal of Metamorphic Geology 16, 309–343.

660 Holland, T. J. B., and R. Powell (2003), Activity-composition relations for phases in petrological
661 calculations: an asymmetric multicomponent formulation, Contributions to Mineralogy
662 and Petrology 145, 492–501.

663 Jackson, J. A., H. Austrheim, D. McKenzie, and K. Priestley (2004), Metastability, mechanical
664 strength, and the support of mountain belts, Geology 32, 625-628.

665 John, T., S. Medvedev, L. H. Ruepke, T. B. Andersen, Y. Y. Podladchikov, and H. Austrheim
666 (2009), Generation of intermediate-depth earthquakes by self-localizing thermal runaway,
667 Nature Geoscience 2, 137-140.

668 Kruse, R., H. Stünitz, and K. Kunze (2001), Dynamic recrystallization processes in plagioclase
669 porphyroclasts, Journal of Structural Geology 23, 1781-1802.

670 Kullerud, K., K. Flaat, and B. Davidsen, (2001), High-pressure Fluid-Rock Reactions involving
671 Cl-bearing Fluids in Lower-crustal Ductile Shear Zones of the Flakstadøy Basic
672 Complex, Lofoten, Norway, Journal of Petrology 42, 1349-1372.

673 Leib, S.E., D.P. Moecher, M.G. Steltenpohl, and A. Andresen, (2016), Thermobarometry of
674 metamorphosed pseudotachylyte and associated mylonite: Constraints on dynamic Co-
675 seismic rupture depth attending Caledonian extension, North Norway, Tectonophysics
676 682, 85-95.

677 Lesne, P., S. C. Kohn, J. Blundy, F. Witham, R. E. Botcharnikov, and H. Behrens (2011),
678 Experimental simulation of closed-system degassing in the system basalt–H2O–CO2–S–
679 Cl, Journal of Petrology 52, 1737–1762.

680 Lin, A., T. Maruyama, A. Stallard, K. Michibayashi, A. Camacho, and K.-i. Kano (2005),
681 Propagation of seismic slip from brittle to ductile crust: Evidence from pseudotachylytes
682 of the Woodroffe thrust, central Australia, Tectonophysics 402, 21-35.

683 Lund, M. G., and H. Austrheim (2003), High-pressure metamorphism and deep-crustal
684 seismicity: evidence from contemporaneous formation of pseudotachylytes and eclogite
685 facies coronas, Tectonophysics 372, 59-83, doi:10.1016/S0040-1951(03)00232-4.

686 Maggi, A., J. A. Jackson, D. McKenzie, and K. Priestley (2000), Earthquake focal depths,
687 effective elastic thickness, and the strength of the continental lithosphere, Geology 28,
688 495-498.

689 Markl, G., B. R. Frost, and K. Bucher (1998), The origin of anorthosites and related rocks from
690 the Lofoten Islands, Northern Norway: I. Field relations and estimation of intrinsic
691 variables, Journal of Petrology 39, 1425-1452.

692 McKenzie, D., and J. N. Brune (1972), Melting on fault planes during large earthquakes,
693 Geophysical Journal of the Royal Astronomical Society 29, 65–78.

694 Menegon, L., P. Nasipuri, H. Stünitz, H. Behrens, and E. Ravna (2011), Dry and strong quartz
695 during deformation of the lower crust in the presence of melt, Journal of Geophysical
696 Research, 116, B10410, doi:10.1029/2011JB008371.

697 Menegon, L., H. Stünitz, P. Nasipuri, R. Heilbronner, and H. Svahnberg (2013), Transition from
698 fracturing to viscous flow in granulite facies perthitic feldspar (Lofoten, Norway),
699 Journal of Structural Geology, 48, 95-112.

700 Menegon, L., F. Fusseis, H. Stünitz, and X. Xiao (2015), Creep cavitation bands control porosity
701 and fluid flow in lower crustal shear zones, Geology, 43, 227-230.
702 doi:10.1130/G36307.1

703 Milke, R., G. Neusser, K. Kolzer, and B. Wunder (2012), Very little water is necessary to make a
704 dry solid silicate system wet, Geology 41, 247-250.

705 Moecher, D. P., and M. G. Steltenpohl (2009), Calculation of rupture depth for an exhumed
706 paleoseismogenic fault from mylonitic pseudotachylyte, Geology 37, 999-1002.

707 Moecher, D. P., and M. G. Steltenpohl (2011), Petrologic evidence for seismogenic slip in
708 extending middle to lower continental crust: Heier's Zone of pseudotachylyte, North
709 Norway, in "Geology of the Earthquake Source - a Volume in Honour of Rick Sibson",
710 Special Publication 359, Geological Society, London, 169-186.

711 Okudaira, T., P. Jeřábek, H. Stünitz, and F. Fusseis, (2015), High-temperature fracturing and
712 subsequent grain-size-sensitive creep in lower crustal gabbros: Evidence for coseismic
713 loading followed by creep during decaying stress in the lower crust?, Journal of
714 Geophysical Research, Solid Earth 120(5), 3119-3141, doi:10.1002/2014jb011708.

715 Okudaira, T., N. Shigematsu, Y. Harigane, and K. Yoshida, (2017), Grain size reduction due to
716 fracturing and subsequent grain-size-sensitive creep in a lower crustal shear zone in the
717 presence of a CO_2-bearing fluid, Journal of Structural Geology 95, 171-187.

718 Pec, M., H. Stünitz, R. Heilbronner, M. Drury, and C. de Capitani (2012), Origin of
719 pseudotachylytes in slow creep experiments, Earth and Planetary Science Letters 355-
720 356, 299-310.

721 Pennacchioni, G. (2005), Control of the geometry of precursor brittle structures on the type of
722 ductile shear zone in the Adamello tonalites, Southern Alps (Italy), Journal of Structural
723 Geology 27, 627–644, doi:10.1016/j.jsg.2004.11.008.

724 Pennacchioni, G., and B. Cesare (1997), Ductile-brittle transition in pre-Alpine amphibolite-
725 facies mylonites during evolution from water-present to water-deficient conditions (Mont
726 Mary nappe, Italian Western Alps), Journal of Metamorphic Geology 15, 777-791.

727 Pennacchioni, G., and N. S. Mancktelow (2007), Nucleation and initial growth of a shear zone
728 network within compositionally and structurally heterogeneous granitoids under

729 amphibolite facies conditions, Journal of Structural Geology 29, 1757-1780,
730 doi:10.1016/j.jsg.2007.06.002.

731 Pennacchioni, G., and E. Zucchi (2013), High-temperature fracturing and ductile deformation
732 during cooling of a pluton: the Lake Edison granodiorite (Sierra Nevada batholith,
733 California), Journal of Structural Geology 50, 54-81, doi:10.1016/j.jsg.2012.06.001.

734 Pittarello, L., G. Pennacchioni, and G. Di Toro (2012), Amphibolite-facies pseudotachylytes in
735 Premosello metagabbros and felsic mylonites (Ivrea Zone, Italy), Tectonophysics 580,
736 43-57, doi: 10.1016/j.tecto.2012.08.001.

737 Rybacki, E., and G. Dresen (2000), Dislocation and diffusion creep of synthetic anorthite
738 aggregates, Journal of Geophysical Research 105, 16017-26036.

739 Steltenpohl, M. G., W.E. Hames, and A. Andresen (2004), The Silurian to Permian history of a
740 metamorphic core complex in Lofoten, northern Scandinavian Caledonides, Tectonics 23,
741 1-23.

742 Steltenpohl, M. G., G. Kassos, and A. Andresen (2006), Retrograded eclogite-facies
743 pseudotachylites as deepcrustal paleoseismic faults within continental basement of
744 Lofoten, north Norway, Geosphere 2, 61-72.

745 Steltenpohl, M. G., G. Kassos, A. Andresen, E. F. Rehnström, and W. E. Hames (2011),
746 Eclogitization and exhumation of Caledonian continental basement in Lofoten, North
747 Norway, Geosphere 7, 1-17.

748 Stünitz, H., A. Thust, R. Heilbronner, H. Behrens, R. Kilian, A. Tarantola, and J. D. Fitz Gerald
749 (2017), Water redistribution in experimentally deformed natural milky quartz single
750 crystals—Implications for H_2O-weakening processes, Journal of Geophysical Research –
751 Solid Earth 122, 866-894, doi:10.1002/2016JB013533.

752 Tajcmanova, L., J.A.D. Connolly, and B. Cesare (2009), A thermodynamic model for titanium
753 and ferric iron solution in biotite, Journal of Metamorphic Geology 27, 153-165.

754 White, J. C. (1996), Transient discontinuities revisited: pseudotachylyte, plastic instability and
755 the influence of low pore fluid pressure on deformation processes in the mid-crust,
756 Journal of Structural Geology 18, 1471-1486.

757 White, J. C. (2012), Paradoxical pseudotachylytes – Fault melt outside the seismogenic zone,
758 Journal of Structural Geology 38, 11-20.

759 Wright, T. J., J.R. Elliott, H. Wang, and I. Ryder (2013), Earthquake cycle deformation and the
760 Moho: Implications for the rheology of the continental lithosphere, Tectonophysics 609,
761 504-523.
762

Lithology	Anorthosite host rock	Pristine pseudotachylyte	Mylonitized pseudotachylyte
Sample	**N13-10B**	**N22**	**N13-10D**
Sample location	0432042 E 7549520 N	0432009 E 7550172 N	0432042 E 7549520 N
SiO_2	53.83	51.37	53.54
TiO_2	0.14	0.32	0.30
Al_2O_3	27.22	25.67	25.11
Fe_2O_{3tot}	1.37	3.98	3.80
MnO	0.02	0.04	0.04
MgO	0.41	1.87	1.86
CaO	10.75	10.85	9.89
Na_2O	4.75	4.25	4.24
K_2O	0.61	0.76	0.92
P_2O_5	0.04	0.04	0.04
Tot	99.14	99.15	99.74
FeO	*n.d.*	*n.d.*	*3.32*
L.O.I.	*0.32*	*0.30*	*0.32*

Table 1. Representative whole rock XRF analysis of anorthosites, of pristine-, and of mylonitized pseudotachylytes. GPS coordinates are relative to WGS84, zone 33W.

Figures

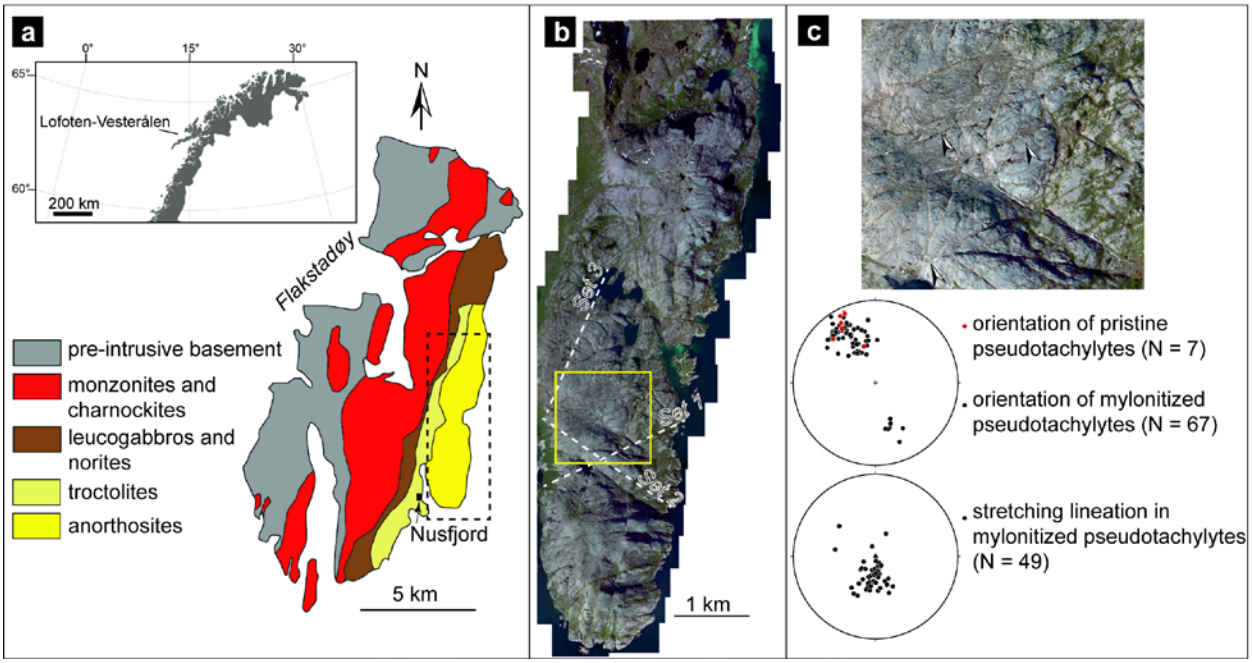

Figure 1. Geological setting. (a) Simplified geological map of Flakstadøy, Lofoten. Modified after Steltenpohl et al. (2006). The dashed rectangle encompasses the area shown in (b). (b) Mosaic of aerial photographs of the Nusfjord ridge. The three main sets of lineaments, defined in the field by ductile shear zones, are marked with white dashed lines. The yellow rectangle encompasses the area shown in (c). (c) Field area investigated in this study. Arrowheads indicate examples of first order shear zones. Pole figures (lower hemisphere, stereographic projection) showing the orientation of set 1 pristine- and mylonitized pseudotachylytes (poles to planes), and of the stretching lineation measured in mylonitized pseudotachylytes. N = number of measurements.

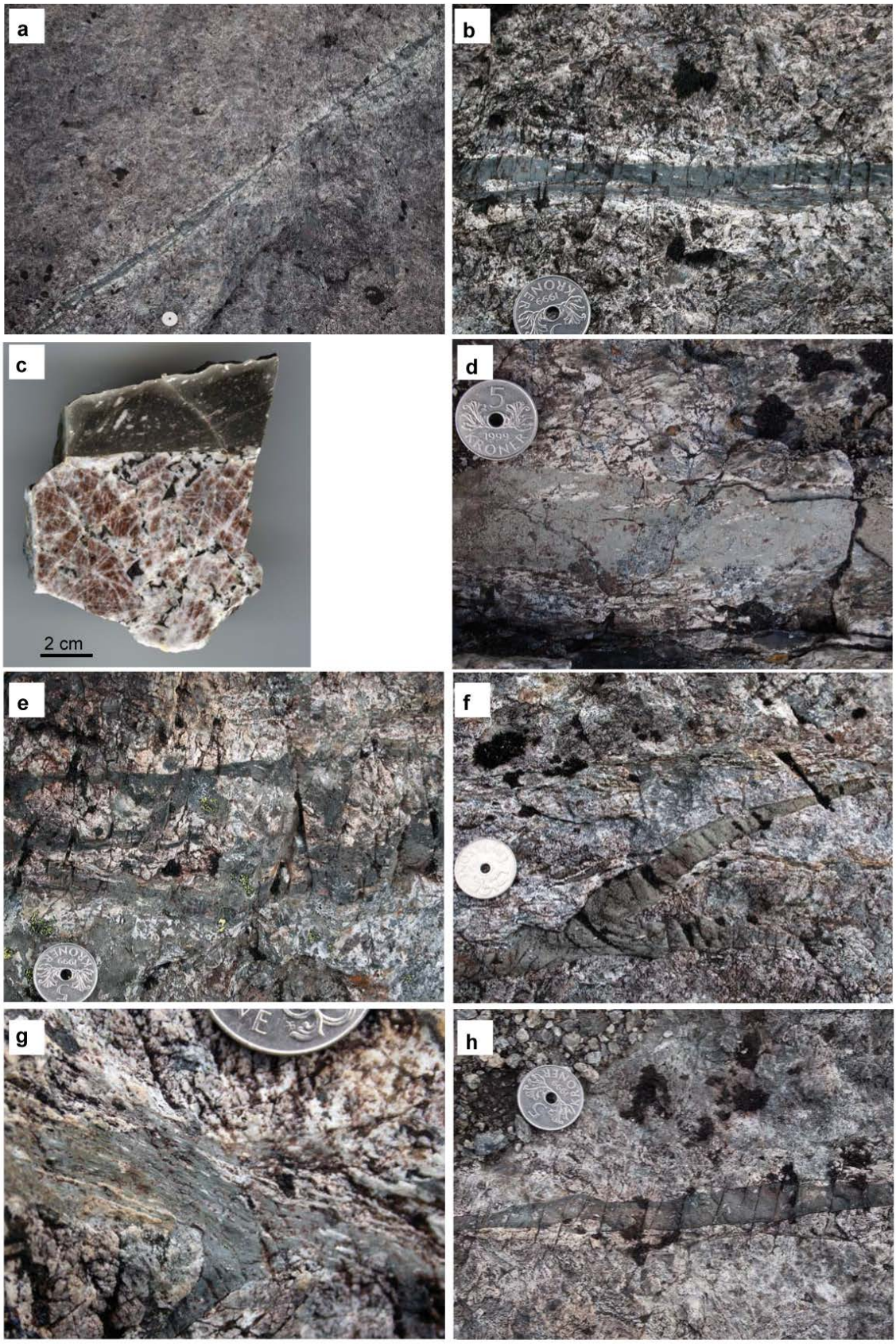
a
b
c
2 cm
d
e
f
g
h

779 **Figure 2.** Field structures of 2nd order shear zones and of pseudotachylyte. All GPS coordinates are relative to
780 WGS84, zone 33W. (a) Thin (<1 cm) ductile shear zone surrounded by a bleached halo within the darker coarse
781 grained anorthosite. GPS coordinates: 0431864 East, 7549944 North. (b) Detail of the shear zone in (a) showing the
782 fine grained, dark green, sharply bounded mylonitic core surrounded by a partially sheared bleached halo. (c)
783 Polished sample of a weakly deformed dark-green shear zone in sharp contact with the host anorthosite. The coarse
784 (cm-sized) purple-coloured magmatic crystals of anorthosite show bleaching along a pervasive network of
785 microfractures. GPS coordinates: 0431685 East, 7549992 North. (d) Relatively weakly deformed pseudotachylyte
786 with lithic clasts of the bleached anorthosite deformed to elongated domains stretched oblique to the
787 pseudotachylyte (shear zone) boundary. Same locality as (c). (e) Pseudotachylyte breccia with bleached lithic clasts
788 and host rock; (f) Pristine pseudotachylyte injection vein protruding from a fault vein; GPS coordinates: 0431808
789 East, 7550038 North. (g) Sheared pseudotachylyte fault vein preserving an undeformed injection vein in the host
790 anorthosite. GPS coordinates: 0432073 East, 7550013 North. (h) Pristine pseudotachylyte preserving chilled
791 margins and small equant clasts of bleached plagioclase. Same locality as (f). Coin for scale (2.5 cm in diameter) in
792 all the field photographs.

793

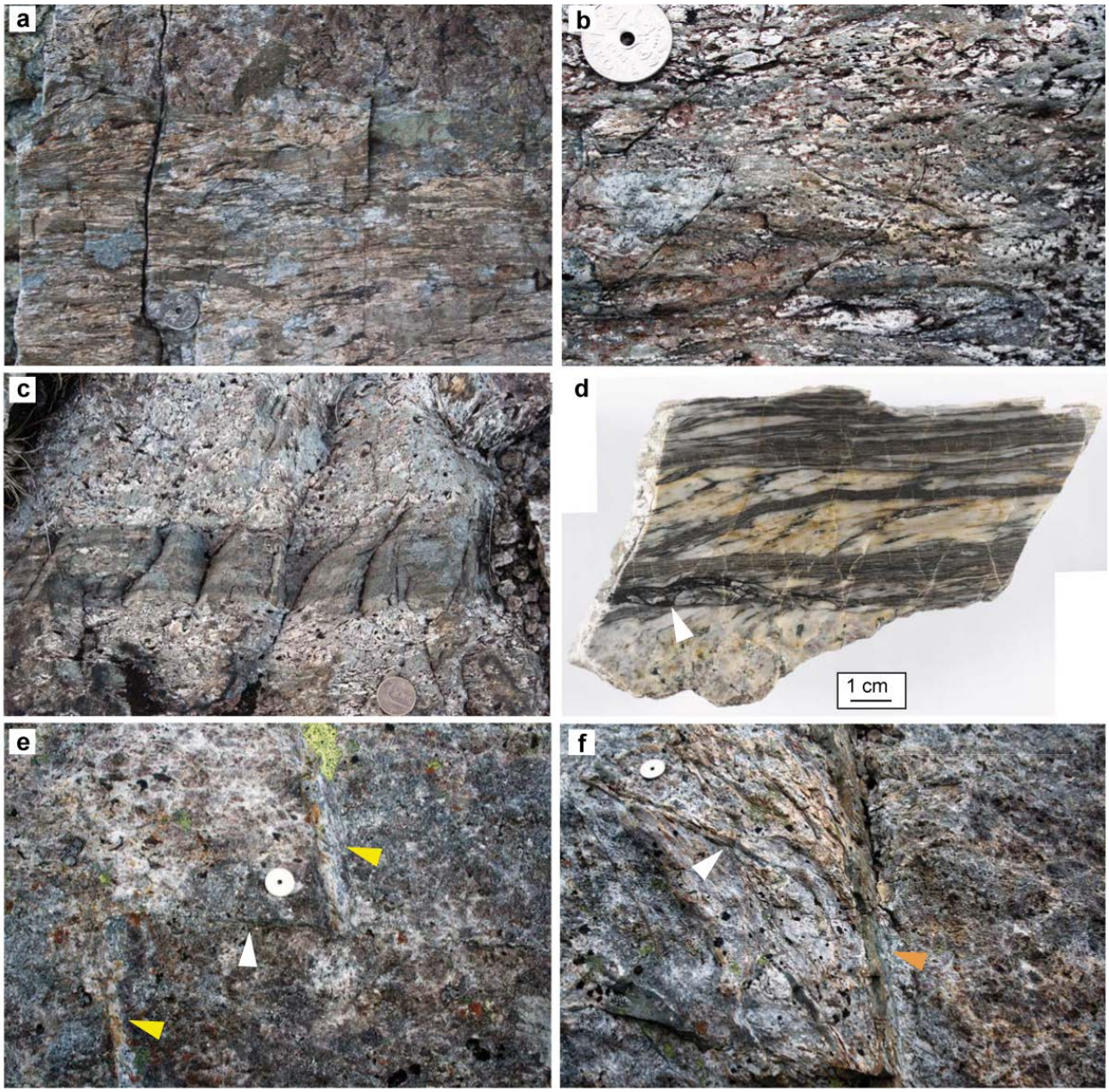

794

795 **Figure 3.** Field structures of major shear zones and associated pseudotachylytes. All GPS coordinates are relative to
796 WGS84, zone 33W. (a) Mylonitic foliation with alternating thin bands of green and whitish colour. Note that some
797 green layers are still locally discordant to the foliation and that pristine pseudotachylyte injection veins are present in
798 the host anorthosite. GPS coordinates: 0432042 East, 7549520 North. (b) Large domain of preserved
799 pseudotachylyte breccia with lithic clast of the bleached host anorthosite free of mylonitic foliation. GPS
800 coordinates: 0432009 East, 7550172 North. (c) Similar as (b) but also showing a thick central pseudotachylyte layer
801 localizing the deformation. Same locality as (b). (d) Polished sample of a domainal foliation delineated by green and
802 whitish layers, derived from pseudotachylyte and bleached anorthosite. In the lower part of the sample, a
803 pseudotachylyte exploited the shear zone boundary and the mylonitic foliation was brecciated within a side wall
804 ripout. Same locality as (a). (e-f) A pristine pseudotachylytes (indicated with a white arrowhead) sharply displaces a
805 withish localized shear zone (yellow arrowheads) (e) and is in turn dragged into the mylonitic foliation along a dm-

thick shear zone with domainal green-whitish layering (orange arrowhead) (f). GPS coordinates: 0432232 East, 7549970 North. Coin for scale (2.5 cm in diameter) in all the field photographs.

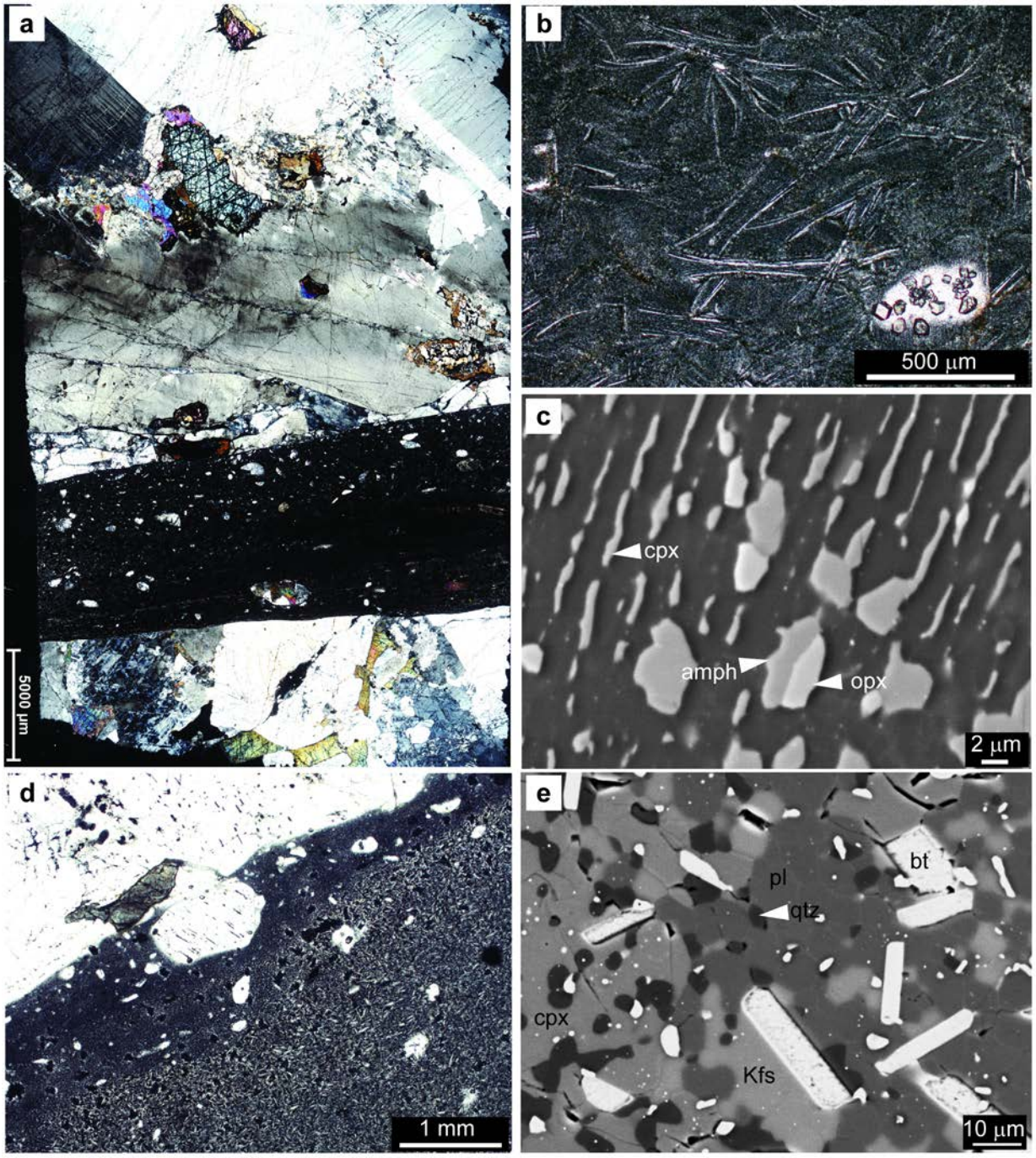

Figure 4. Representative microstructures of pristine pseudotachylytes. Mineral abbrebaviations: amph = amphibole, bt = biotite, cpx = clinopyroxene, Kfs = K-feldspar, pl = plagioclase, qtz = quartz. (a) Thin section of a pristine pseudotachylyte vein and of the anorthosite host rock. Crossed polarizers. (b) Plagioclase survivor clast and microlitic microstructure. Note the cluster of garnet grains overgrowing the plagioclase survivor clast. Parallel polarizers. (c) SEM backscatter electron image of microlites of clinopyroxene, orthopyroxene, amphibole and

plagioclase (dark grey phase). (d) Example of chilled margin of a pseudotachylyte vein. Parallel polarizers. (e) SEM backscatter electron image of the fine-grained phase mixture found in the recrystallized pseudotachylytes.

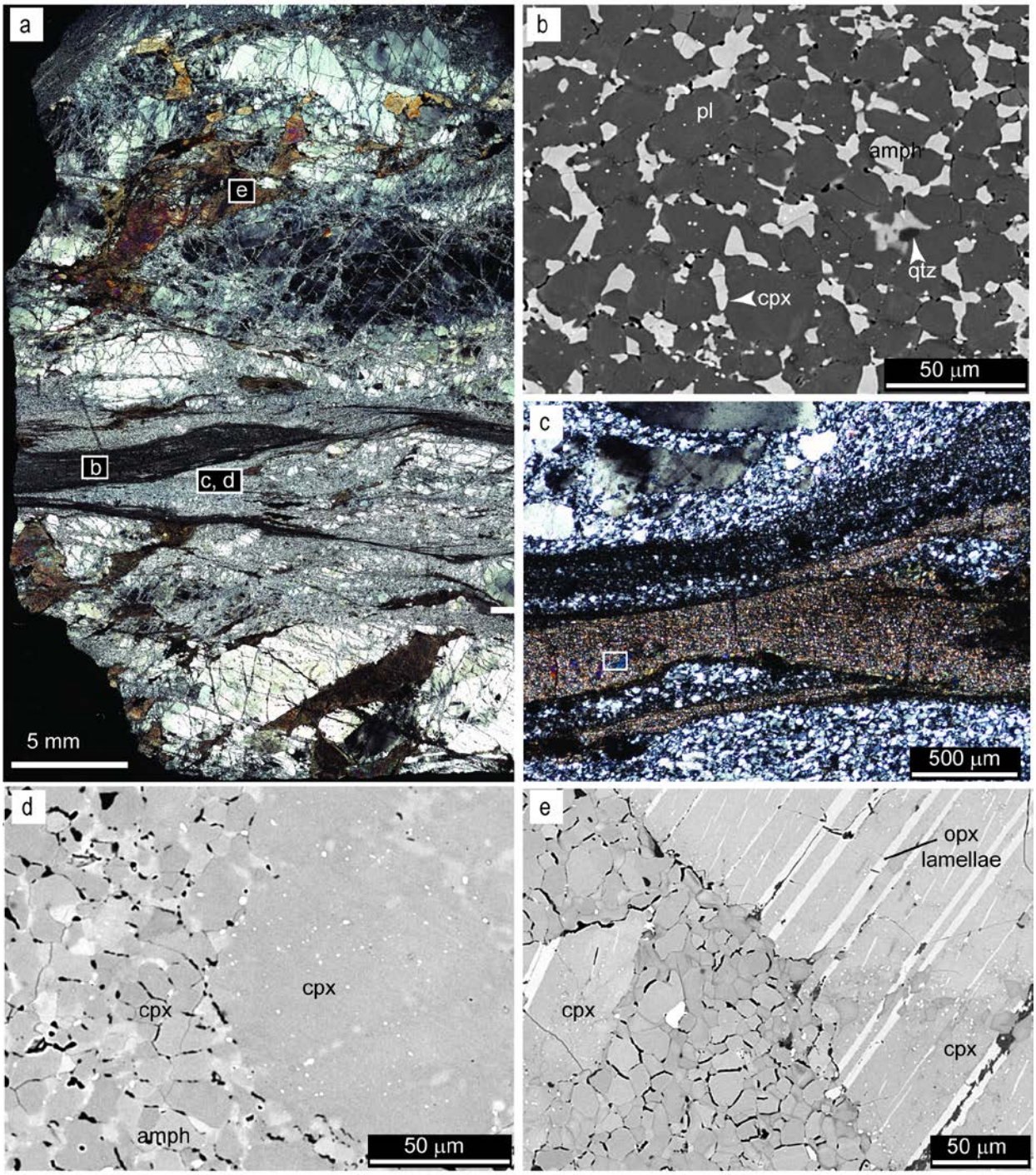

Figure 5. Representative microstructures of ductile shear zones. Mineral abbreviations like in Fig. 4. (a) Thin section of a ductile shear zone consisting of mylonitized pseudotachylytes (transposed and sheared dark veins) and of variably fractured and recrystallized anorthosite. Black rectangles show the microstructural position of figures 5b-5e. Crossed polarizers. (b) SEM backscatter electron image of the fine-grained mylonitized pseudotachylyte vein shown in (a). (c) Bands of recrystallized plagioclase (with relict fragments of magmatic grains) alternating with clinopyroxene-derived aggregate (brown band) along the shear zone foliation. The clinopyorexene-derived

aggregate consists of clinopyroxene porphyroclasts embedded in a fine-grained matrix of clinopyroxene, amphibole and quartz. Light microscope image, crossed polarizers. The white rectangle shows the approximate position of Fig. 5d. (d) SEM backscatter electron image of a detail of the site shown in (c). (e). Fractured clinopyroxene in the amage zone flanking the shear zone. The intracrystalline fracture is filled with small grains of clinopyroxene and amphibole.

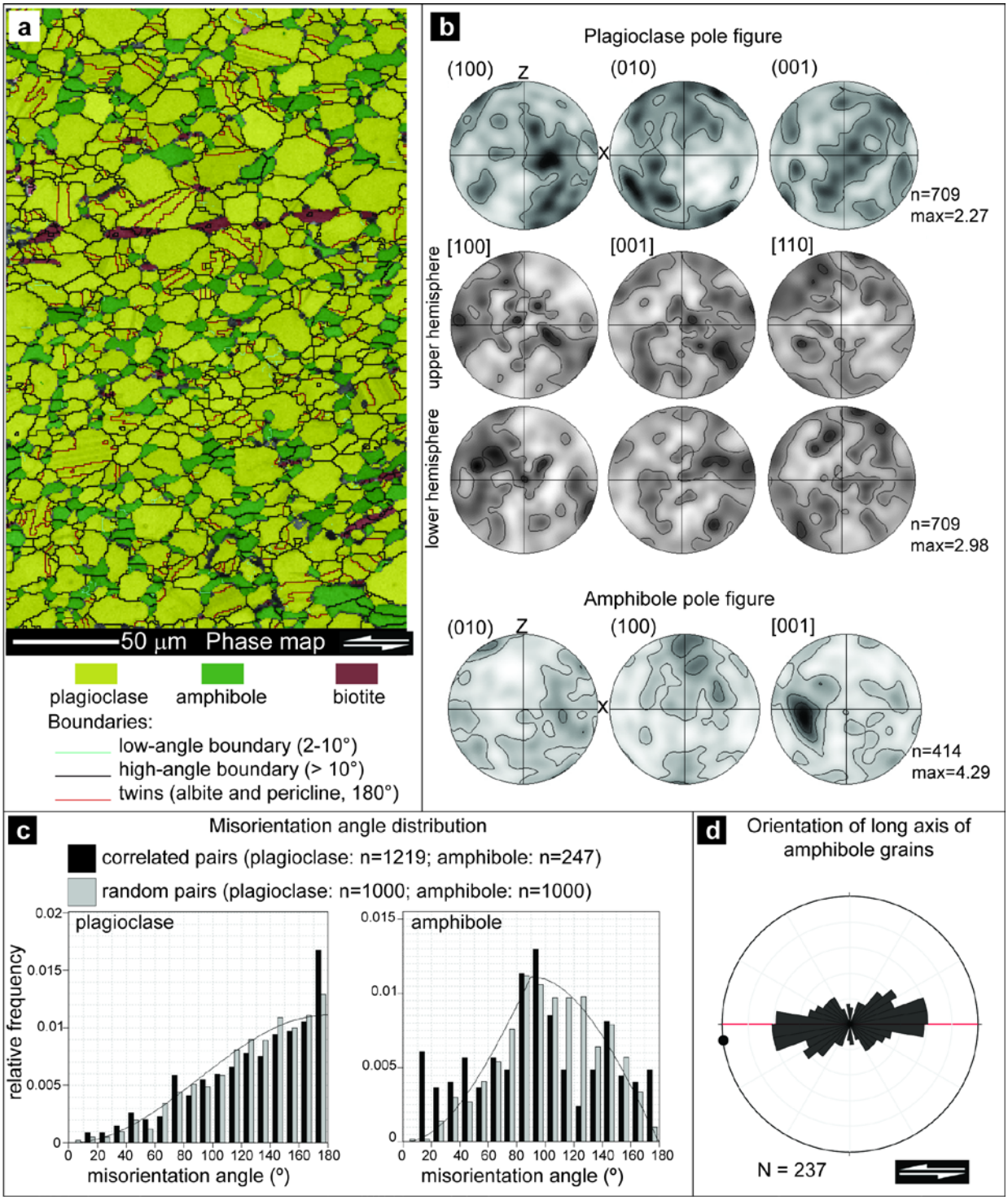

Figure 6. EBSD analysis of a mylonitized pseudotachylyte vein. (a) Phase map of a fine-grained mylonitized pseudotachylyte. (b) Contoured pole figures (half width 15°, data clustering 5°) of plagioclase and amphibole from

831 the site shown in (a), plotted as one point per grain (n = number of grains). Black colour marks maxima, also given
832 as multiples of the uniform distribution. (c) Histograms of misorientation axis distribution of plagioclase and
833 amphibole form the site shown in (a). The theoretical curves for a random orientation are also shown. (d) Rose
834 diagram showing the orientation of the long axis of amphibole grains included in (a). The red line is parallel to the
835 trace of the shear zone boundary.

836

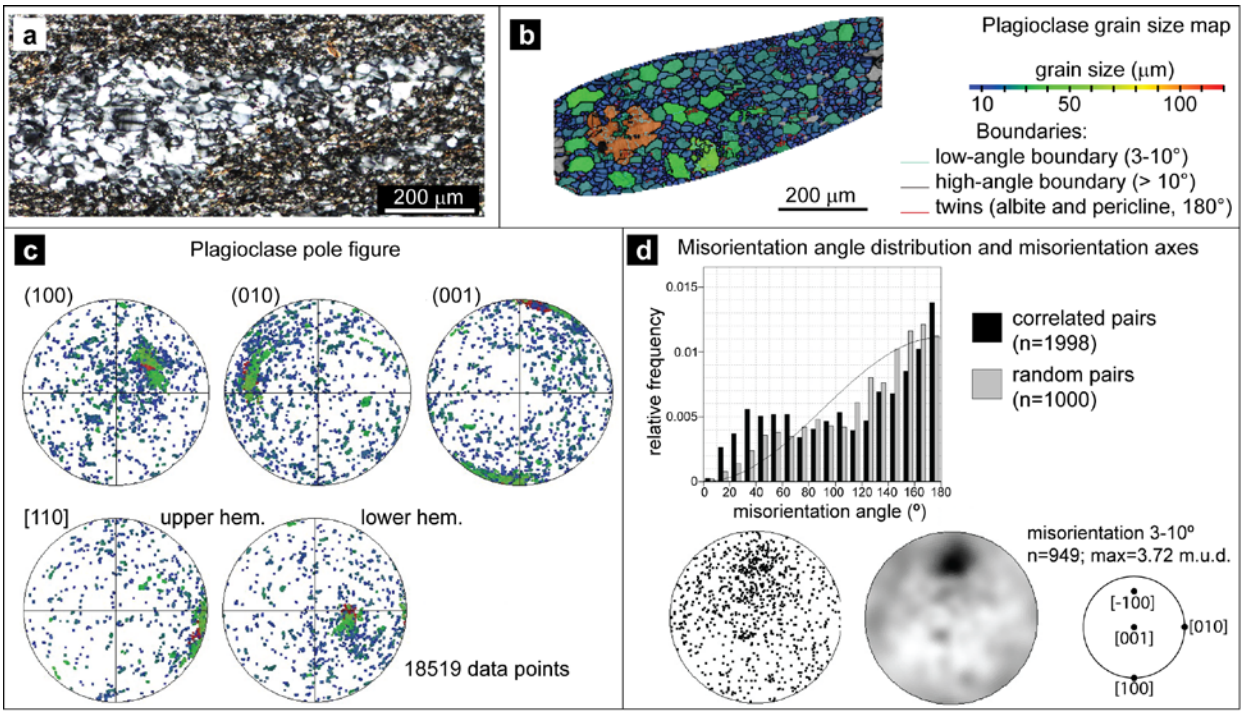

Figure 7. EBSD analysis of a recrystallized plagioclase aggregate embedded in a mylonitized pseudotachylyte vein. (a) Microstructure of the analysed aggregate. Crossed polarizers. (b) Grain size map of the plagioclase aggregate shown in (a). The large grain color-coded orange in interpreted as a relict fragment of the primary plagioclase grain. (c) Plagioclase pole figure of the grains included in (b), and colour coded like the grain size map shown in (b). (d) Misorientation angle distribution histogram of plagioclase and misorientation axis for misorientations of 3-10° plotted in crystal coordinates, both as point data and as contoured plot. The theoretical curve for a random distribution is also shown.

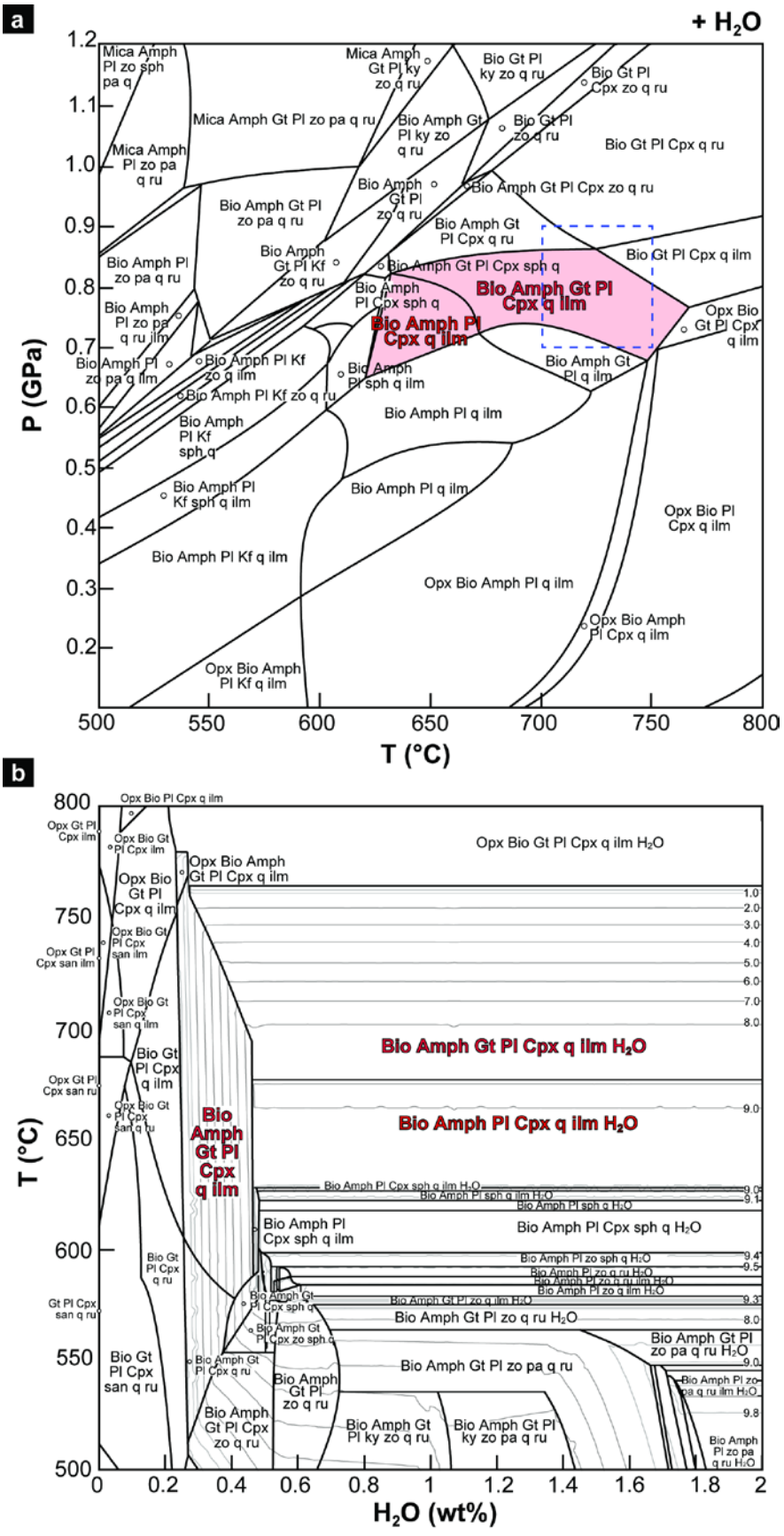
a
+ H2O
P (GPa)
T (°C)
Mica Amph Pl zo sph pa q
Mica Amph Gt Pl ky zo q ru
Bio Gt Pl ky zo q ru
Bio Gt Pl Cpx zo q ru
Mica Amph Gt Pl zo pa q ru
Bio Amph Gt Pl ky zo q ru
Bio Gt Pl zo q ru
Bio Gt Pl Cpx q ru
Mica Amph Pl zo pa q ru
Bio Amph Gt Pl zo pa q ru
Bio Amph Gt Pl zo q ru
Bio Amph Gt Pl Cpx zo q ru
Bio Amph Gt Pl Cpx q
Bio Amph Gt Pl Kf zo q ru
Bio Amph Gt Pl Cpx sph q
Bio Gt Pl Cpx q ilm
Bio Amph Pl zo pa q ru
Bio Amph Pl Cpx sph q
Bio Amph Gt Pl Cpx q ilm
Bio Amph Pl zo pa q ru ilm
Bio Amph Pl Cpx q ilm
Opx Bio Gt Pl Cpx q ilm
Bio Amph Pl zo pa q ilm
Bio Amph Pl Kf zo q ilm
Bio Amph Pl sph q ilm
Bio Amph Gt Pl q ilm
Bio Amph Pl Kf zo q ru
Bio Amph Pl Kf sph q
Bio Amph Pl q ilm
Bio Amph Pl Kf sph q ilm
Opx Bio Pl Cpx q ilm
Bio Amph Pl Kf q ilm
Opx Bio Amph Pl q ilm
Opx Bio Amph Pl Cpx q ilm
Opx Bio Amph Pl Kf q ilm
b
H2O (wt%)
T (°C)
Opx Bio Pl Cpx q ilm
Opx Gt Pl Cpx ilm
Opx Bio Gt Pl Cpx ilm
Opx Bio Gt Pl Cpx q ilm H2O
Opx Bio Amph Gt Pl Cpx q ilm
Opx Bio Gt Pl Cpx q ilm
Opx Bio Gt Pl Cpx san ilm
Opx Gt Pl Cpx san ilm
Opx Bio Gt Pl Cpx san q ilm
Bio Amph Gt Pl Cpx q ilm H2O
Bio Gt Pl Cpx q ilm
Opx Gt Pl Cpx san ru
Opx Bio Gt Pl Cpx san q ru
Bio Amph Pl Cpx q ilm H2O
Bio Amph Gt Pl Cpx q ilm
Bio Amph Pl Cpx sph q ilm H2O
Bio Amph Pl sph q ilm H2O
Bio Amph Pl sph q H2O
Bio Amph Pl Cpx sph q ilm
Bio Amph Pl Cpx sph q H2O
Bio Amph Pl zo sph q H2O
Bio Amph Pl zo q ru H2O
Bio Amph Pl zo q ru ilm H2O
Bio Amph Pl zo q ilm H2O
Bio Gt Pl Cpx q ru
Bio Amph Gt Pl Cpx sph q
Bio Amph Gt Pl zo q ilm H2O
Gt Pl Cpx san q ru
Bio Amph Gt Pl zo q ru H2O
Bio Amph Gt Pl Cpx zo sph q
Bio Amph Gt Pl zo pa q ru H2O
Bio Gt Pl Cpx san q ru
Bio Amph Gt Pl Cpx q ru
Bio Amph Gt Pl zo pa q ru
Bio Amph Gt Pl zo q ru
Bio Amph Pl zo pa q ru ilm H2O
Bio Amph Gt Pl Cpx zo q ru
Bio Amph Gt Pl ky zo q ru
Bio Amph Gt Pl ky zo pa q ru
Bio Amph Pl zo pa q ru H2O

847 **Figure 8.** (a) Isochemical *P–T* section for mylonitized pseudotachylyte calculated in the system SiO_2 (53.03) –
848 Al_2O_3 (24.84) – MgO (1.87) – CaO (9.96) – Na_2O (4.24) – K_2O (0.89) – TiO_2 (0.31) – FeO (3.32) – Fe_2O_3 (0.11).
849 Values in brackets are oxide wt.%. The red area shows the hypothetical stability field of the mylonite paragenesis, as
850 evidenced by microstructural and mineral chemistry analyses. Abbreviations for solid solution models: Amph –
851 amphiboles; Bio – biotite; Cpx – clinopyroxene; Gt – garnet; Kfs – alkali feldspar; Mica – phengite; Pl – ternary
852 feldspar. Abbreviations for phases: zo – zoisite; sph – titanite (sphene); q – quartz; pa – paragonite; ky – kyanite; ru
853 – rutile; ilm – ilmenite. The dashed blue rectangle shows the P, T conditions estimated with amphibole-plagioclase
854 geothermobarometry. (b) Isochemical T-H_2O section (same composition) calculated at 0.7 GPa, showing the stable
855 paragenesis from dry conditions up to 2 wt% of water. In the temperature range of interest (600-750 °C) the system
856 becomes H_2O saturated (i.e. free water) when the H_2O of the bulk composition is higher than 0.3-0.5 wt%
857 (depending on the temperature). The grey lines and the corresponding numbers on the right-hand side of the plot
858 indicate the amount of amphibole (vol%) occurring in the mineral assemblage.

859

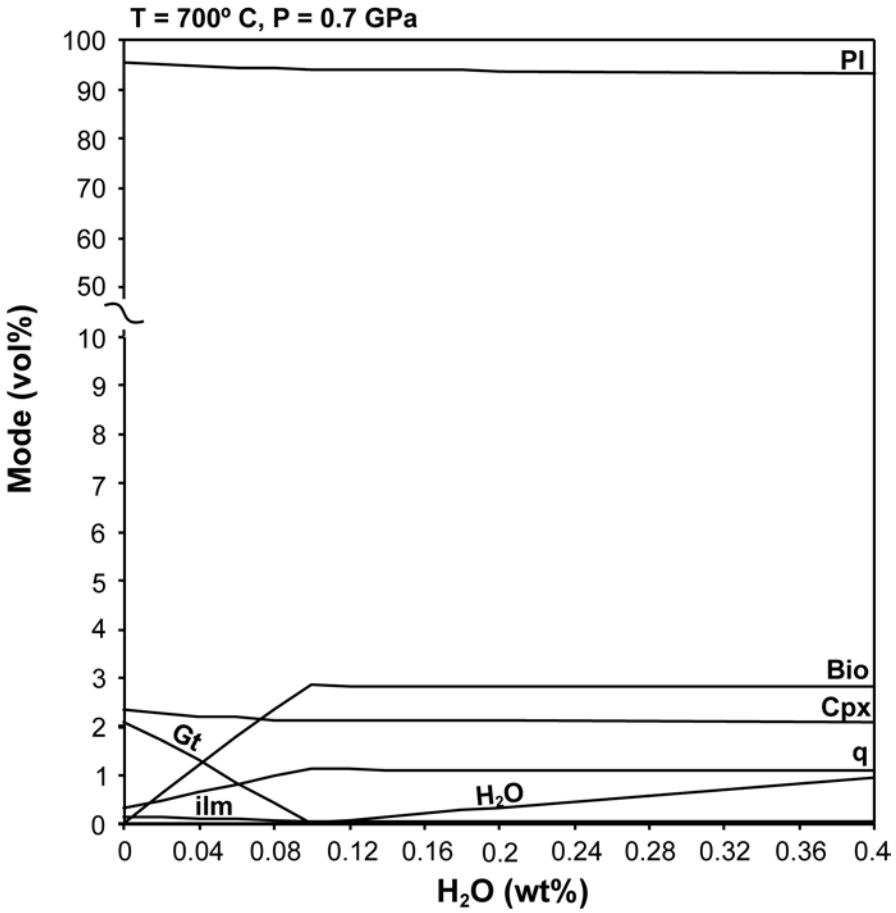

860

861 **Figure 9.** Modal phase abundances (vol%) of the isochemical section calculated at 0.7 GPa and 700 °C for the
862 pristine anorthosite, calculated in the system SiO_2 (53.83) – Al_2O_3 (27.22) – MgO (0.41) – CaO (10.75) – Na_2O
863 (4.75) – K_2O (0.61) – TiO_2 (0.14) – FeOtot (1.23)**.** Mineral and solid solution abbreviations are the same as in Fig.8.

864

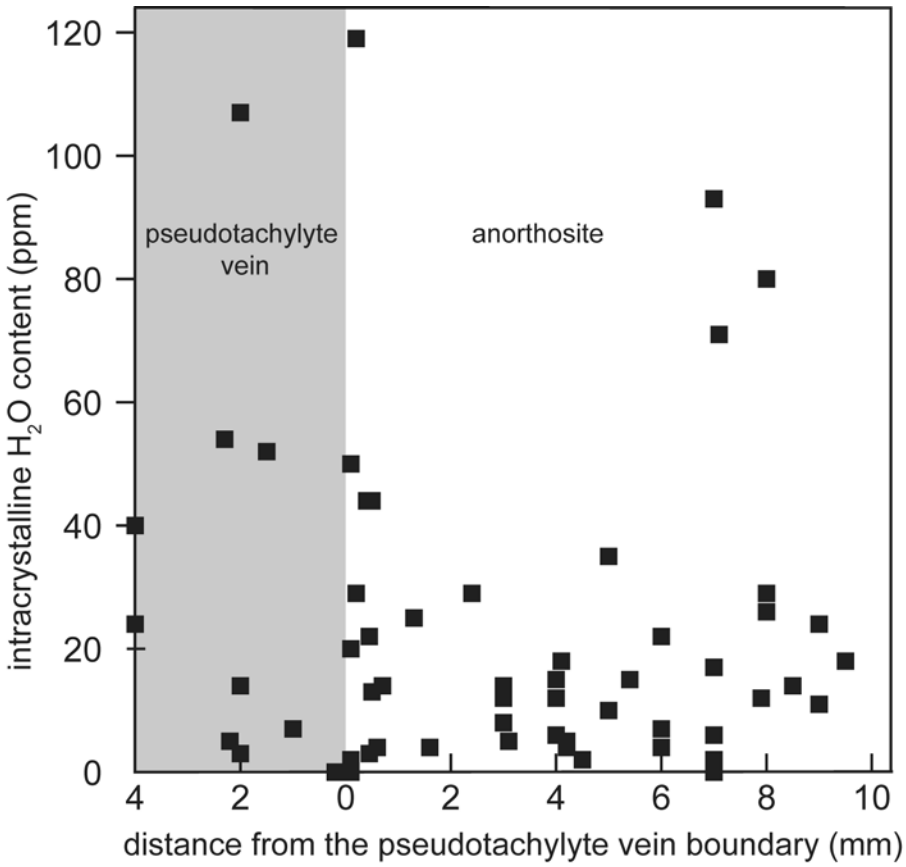

Figure 10. Results of the ion microprobe measurements of intracrystalline water content in plagioclase. The area shaded in grey corresponds to the interior of a pristine pseudotachylyte vein.

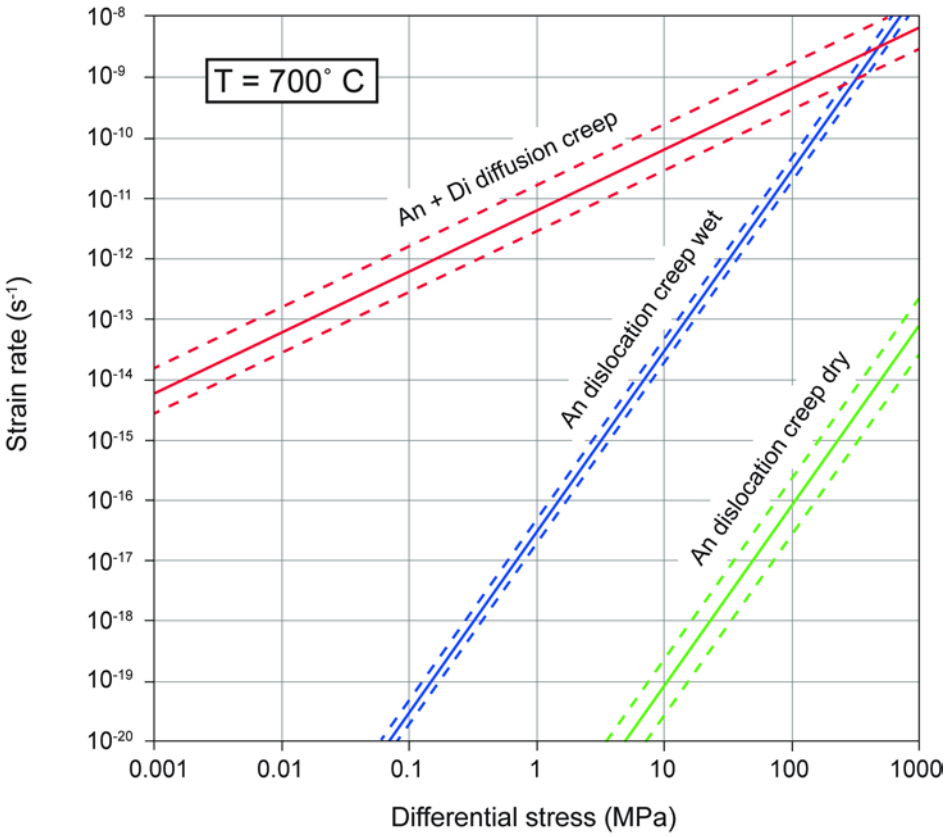

Figure 11. Plot of strain rate (s^{-1}) versus differential stress (MPa) to model the rheology of the mylonitized pseudotachylytes at a temperature of 700°C. The following flow laws were used: anorthite + diopside wet diffusion creep (the $An_{25}Di_{35}W$ flow law of Dimanov and Dresen, 2005), anorthite wet dislocation creep (Rybacki and Dresen, 2000; water content = 0.07 wt%), anorthite dry dislocation creep (Rybacki and Dresen, 2000; water content = 0.004 wt%). Dashed lines represent uncertainties in the pre-exponential term *A* and in the activation energy *Q* of each flow law. We used the average stress exponents derived experimentally (n = 1 for the diffusion creep flow law, n = 3 for the dislocation creep flow laws).